Heat and Mass Transfer Modeling and Experimental Validation of a Novel Freeze Desalination Process

Ethan Allen Wise

Thesis submitted to the faculty of the Virginia Polytechnic Institute and State University in partial fulfillment of the requirements for the degree of

Master of Science

In

Mechanical Engineering

Michael W. Ellis

Michael R. von Spakovsky

Scott T. Huxtable

May 24, 2021

Blacksburg, Virginia

Keywords: Desalination, Freeze Concentration, Thermal Separation

Heat and Mass Transfer Modeling and Experimental Validation of a Novel Freeze Desalination Process

Ethan Allen Wise

ABSTRACT

Freeze concentration is a thermal separation process that is used to purify aqueous solutions. One application of recent interest is seawater desalination. For freeze concentration to be an effective desalination method, a high ice growth rate and product purity must be achieved with energy usage comparable to that of competing technologies.

The purpose of this thesis is to develop a coupled heat and mass transfer model to predict the growth rate and purity of the solid phase for ice grown about a horizontal, immersed tube. By simultaneously solving the heat and mass transfer problems, this model improves upon previous attempts found in the literature. In addition, an experimental apparatus was constructed and a series of ten experiments was run, considering a range of cooling rates, process times, and saltwater concentrations. Average ice growth velocities ranged from 3.1-13.1 mm/h and the observed partition coefficient ranged from 0.42-0.71. The model was calibrated using experimental data, and the coefficients of variation for the fitted model's prediction of ice mass and capture concentration were 15.4% and 7.6% respectively. Based on insights from modeling and experimentation, a series of suggestions are made regarding future modeling and process design.

Heat and Mass Transfer Modeling and Experimental Validation of a Novel Freeze Desalination Process

Ethan Allen Wise

GENERAL AUDIENCE ABSTRACT

Freeze concentration is a thermal process that is used to purify a liquid containing dissolved solids. One application of recent interest is seawater desalination. For freeze concentration to effectively purify seawater, a high ice growth rate and product purity must be achieved with energy usage comparable to that of competing technologies.

The purpose of this thesis is to develop a coupled heat and mass transfer model to predict the growth rate and purity of the solid phase for ice grown about a horizontal, immersed tube. By simultaneously solving the heat and mass transfer problems, this model improves upon previous attempts found in the literature. In addition, an experimental apparatus was constructed and a series of ten experiments was run, considering a range of cooling rates, process times, and saltwater concentrations. Average ice growth velocities ranged from 3.1-13.1 mm/h and the salinity of the ice ranged from 0.42-0.71% of the original concentration. Based on insights from modeling and experimentation, a series of suggestions are made regarding future modeling and process design.

TABLE OF CONTENTS

LIST OF FIGURES

LIST OF TABLES

Chapter 1

MOTIVATION AND INTRODUCTION TO FREEZE CONCENTRATION

The purpose of this work is to develop and validate a heat and mass transfer model of a novel freeze desalination process. The primary goals of the model are the successful prediction of the ice growth rate, ice purity, and process energy consumption. In this chapter, the research objective is defined and motivated. Prominent desalination technologies will be reviewed, as will the physical principles behind freeze concentration. A literature review will be presented, considering previous experimental and modeling attempts of freeze concentration. The introduction will conclude with an outline of the remaining chapters.

1.1 Desalination as a Potential Solution to a Rising Freshwater Demand

Due to a globally increasing freshwater demand and the continuous depletion of current sources, effective seawater desalination will likely become a crucial component of future freshwater supply. Over recent decades, global water use has consistently and significantly increased [1]. This trend is partially due to the rising population and partially due to improvements in living standards related to factors such as industrialization, sanitation, and agriculture. In the twentieth century, water usage increased by a factor of 6 while the global population tripled, suggesting that, while population plays a larger role than per-capita usage, both factors have significantly contributed to the increase water usage [2]. Because global living standards continue to rise and population growth is expected to persist, it is reasonable to conclude that freshwater demand will continue to increase throughout the current century.

At the same time, many freshwater sources are being utilized at unsustainable rates. For sources such as lakes, rivers, and groundwater, replenishment is based on precipitation and, over the course of years, occurs at roughly a fixed rate within a given region. When the rate at which a source is utilized exceeds the replenishment rate, the result is an imbalance in the local water cycle. It is estimated that over 29% of the world's population lives in water-stressed regions [1]. Despite localized imbalances in the water cycle, water is an abundant and conserved quantity. A portion of the net water transfer is to the ocean which contains 97% of the globe's water [3]. Because the ocean's supply is effectively limitless, large-scale desalination would solve the looming freshwater shortage. Additionally, since the majority of the population lives in coastal areas, large-scale desalination would likely reduce the required level of distribution [4].

The primary obstacles to desalination are expense and scalability. Expense is closely tied to energy usage and capital, while scalability depends on process speed and the associated equipment. It is also important that sufficient purification is achieved. Seawater has a salinity of approximately 35 ppt, but the acceptable salinity of the purified water is application dependent [1]. For example, the EPA advises that drinking water should not exceed a salinity of 0.15 ppt [5]. However, the salinity of irrigation water can be as high as 3.2 ppt without adversely affecting the yield of crops such as barley and wheat [6]. Thus, through strategic distribution of various water supplies, it is possible to combat shortages with even partially purified water.

Desalinated water currently accounts for about 1% of global water consumption, but capacity continues to increase [1,3]. This water is primarily desalinated using either membrane-based separation methods (67%) or thermal separation methods (33%) [7].

Reverse osmosis, the primary membrane separation method, uses semipermeable membranes to block the transport of dissolved salts. This process, illustrated in Figure 1.1, begins by filtering debris and other large particles out of the intake stream. The initial filtering is followed by a series of chemical treatments intended to prevent downstream scaling and membrane fouling [8]. The specific treatments are dependent upon feedwater composition. Next, the solution is pumped to a high pressure before passing through microporous membranes. To overcome the osmotic pressure, the solution is pumped to a pressure of up to 80 bar [8]. Osmotic pressure is the pressure required to prevent the diffusion of a pure solvent towards the solution side of a membrane, and is dependent on the salinity of said solution. After separation occurs, the concentrated brine is rejected to the source. Because the rejected brine is still at a high pressure, turbines are often used to harvest energy from the outlet stream. The recovery rate of purified water is about 75% of the intake volume [9].

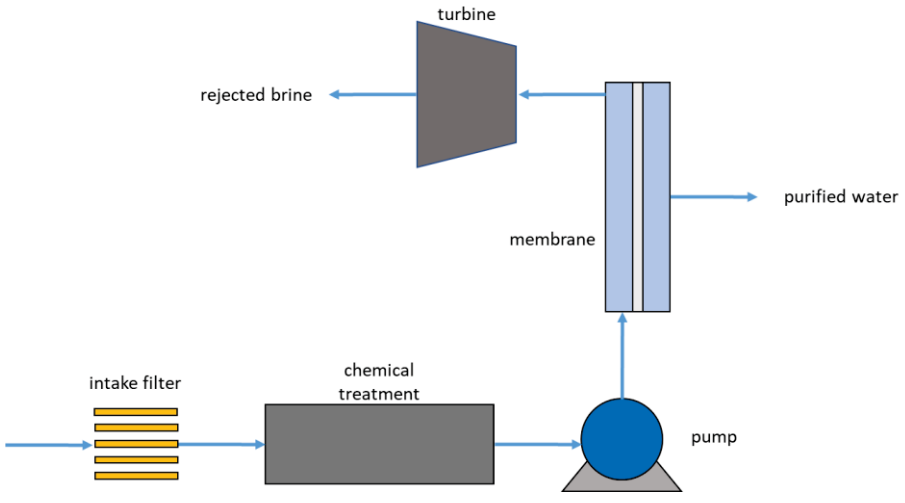

Figure 1.1: Diagram of the reverse osmosis process.

Reverse osmosis is becoming the dominant desalination technology due to its low energy requirement. Because the required pressure depends upon the salinity of the source

water, energy usage is largely dependent upon whether brackish or sea water is processed. Large plants can process seawater as efficiently as 3 kWh/m^3 [7]. One disadvantage of reverse osmosis is that capital costs can be quite high and are on-par with energy costs [10]. Additionally, the membranes deteriorate and become fouled over time, leading to regular maintenance.

Of the various thermal separation methods, multi-stage flash (MSF) currently represents the largest capacity [2]. In the MSF process, incoming saline water is heated until it reaches a temperature near the concentration dependent boiling point. The high temperature solution then passes through a series of chambers held at vacuum pressures. The pressures, successively lower in each chamber, are such that a portion of the heated solution evaporates in each chamber. This now-pure water vapor rises and condenses on coils which contain incoming saline solution. In this way, the enthalpy of vaporization is recycled, improving the energy efficiency of the process. However, a separate brine heater is still required to provide additional thermal energy. The condensed, desalinated water is collected before exiting the process.

Despite water's high enthalpy of vaporization of 2500 kJ/kg, multi-stage flash's re-use of this energy leads to high efficiencies when many stages are included in the process. For a plant with 20 stages, the thermal energy requirement is only about 290 kJ/kg or 81 kWh/m^3 of desalinated water [3]. While this energy requirement far exceeds that of reverse osmosis, this requirement is for thermal energy instead of electrical energy. MSF is particularly attractive when excess thermal energy is regularly available. For example, MSF plants are often installed alongside thermal power plants which provide waste heat

in the form of steam. The MSF process also requires less maintenance than reverse osmosis, although corrosion can occur at the high operating temperatures.

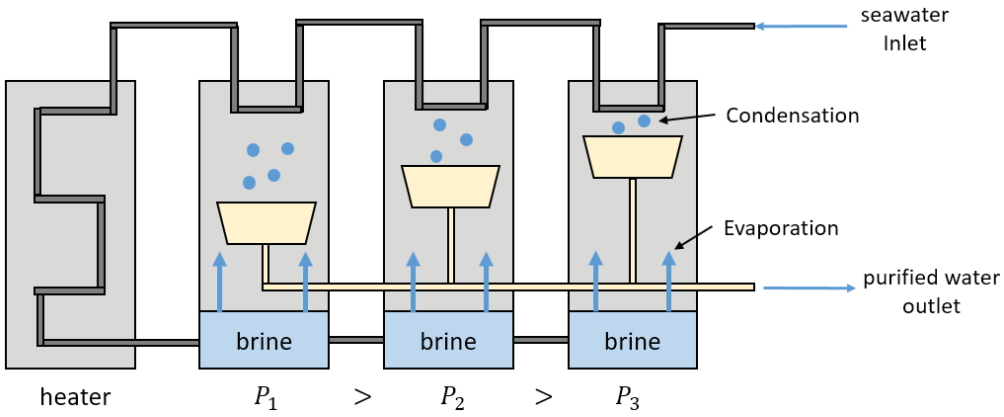

Figure 1.2: Diagram of the MSF process.

1.2 Freeze Concentration Process Overview

Freeze concentration (FC), another means of separating solutions, utilizes the solidification process to produce a relatively pure solid phase. It is a well-documented phenomenon that impurities tend to be rejected during crystallization. This is because for most substances, including water, a perfect lattice corresponds to a lower energy state than a lattice possessing impurities. Thus, intermolecular forces contribute to solute rejection [11]. If sufficiently slow growth of an even crystal front is maintained, the solute rejecting forces dominate and a relatively pure solid is formed. Once the freezing process is complete, the ice can be separated and melted to achieve a pure solution.

There are many variations of the fundamental FC process. Indirect freeze concentration, which involves direct contact between the solution and a water-immiscible refrigerant, is energy efficient but is subject to contamination concerns [1]. In falling film freeze

concentration (FFFC), a thin stream of liquid is sprayed across a cooled plate, allowing an ice layer to form. After sufficient growth is achieved, the plate is scraped to collect the ice [4]. Static layer crystallization, also referred to as indirect freezing, involves the freezing of ice about a heat exchanger which is immersed in a stagnant bath. Previously considered geometries include a vertical cylinder and flat plates [12,13].

Current FC applications include the processing of food concentrates and drug separation [14]. There is also interest in using FC as a desalination technique, but, to date, no industrial-scale plants have been built [1]. From a comparative viewpoint, FC has an inherent advantage over distillation methods because, for water, the enthalpy of fusion is about 1/7 the heat of vaporization. Given that the enthalpy of fusion for water is 92.5 kWh/m^3 and assuming a pre-freeze cooling of 20 C and a coefficient of performance of 5, a single stage freeze desalination process would produce ice at an energy cost of about 22.9 kWh/m^3. While not inordinately energy intensive, this process could not compete with reverse osmosis. However, if a series of stages, like those of the MSF process, was used, the effective energy requirement could be substantially lowered. Unlike reverse osmosis, freeze desalination is not susceptible to fouling and requires less regular maintenance. A significant challenge posed by FC is process speed. To form high purity crystals, ice growth must occur slowly. Further, FC is not conducive to a continuous flow process, as the frozen water must slowly melt and is not easily moved. Additionally, the relationship between purity and production rate of ice is not well documented and freeze desalination largely remains in the realm of research.

Due to variability in energy and labor costs, regulations, plant size, plant lifetime, and feed water conditions, it is very difficult to compare the capital and maintenance costs of

MSF, RO, and FC. Additionally, because industrial-scale freeze desalination plants do not yet exist, one must rely on projections rather than case studies. However, Williams et al., after collecting and averaging reported costs, provided an estimate of the total cost per unit volume for each of these desalination technologies [15]. Their findings are reported in Table 1.1. The cost estimates for freeze desalination were based on process modeling as well as metrics from freeze concentration processes in the food industry. The electrical energy use for MSF was based on a power plant efficiency of 30% and the electrical energy use for FC was based on a refrigeration cycle with a COP of 5.

Table 1. 1: Energy and total cost for various desalination technologies.

	Heat Transfer, kWh/m3.	Electrical Energy, kWh/m3.	Total cost, USD/m3 [15].
MSF	81	24.3	1.16
RO	-	3	0.66
FC	114.7	22.9	0.93

1.3 Freeze Desalination Literature Review

An early attempt to model static layer crystallization was made by Wollhover et al. [16]. This one-dimensional, coupled heat and mass transfer model considered the freezing of a saltwater bath between two parallel plates. The bath was initially at a uniform temperature, and the plates were held at a specified, time-dependent temperature. The solid phase grew uniformly and equally off each plate, and the heat equation was solved in both phases with symmetry dictating a zero heat-flux at the midpoint of the liquid phase. A concentration-dependent temperature of solidification was imposed at the solid-liquid interface for both phases, linking the temperature and concentration solutions. Because the heat equation was solved in both phases, a non-zero net heat flux exists

across the interface. The growth rate of the ice front was determined by enforcing conservation of energy across the interface, resulting in a moving boundary condition. To determine the interfacial concentration, the diffusion equation was solved in the liquid phase. At the midpoint of the bath, a zero-flux boundary condition was applied. At the solid-liquid interface, zero-capture was assumed. Therefore, the convective flux, based upon the interfacial velocity, was equated with the diffusive flux. Due to the interconnectedness of temperature, concentration, and velocity, an iterative scheme was developed to yield the numerical solution at each timestep. This study proposed a well-developed heat transfer model which relates the ice growth rate and interfacial temperature to the concentration profile. However, the zero-capture assumption is not realistic, and the model is not helpful for predicting the capture which is observed to occur in freeze concentration.

A more recent study, by Chen and Wu, formulated an analytical model for solute capture in freeze concentration processes [17]. In this work, no heat transfer model was considered, and an interfacial velocity was simply assumed. Beginning with the one-dimensional convection-diffusion concentration equation, a quasi-steady state was assumed so that transient effects could be neglected. A boundary layer profile was assumed where the interfacial concentration in the liquid is $C_{i,sw}$, and the free-stream concentration is C_{sw}. The assumed functional form for the interfacial concentration is given in Eq. 1.1 where A and n are constants, v is the interfacial velocity, δ is the concentration boundary layer thickness, and D is the solute diffusion coefficient.

$$\frac{C_{i,sw}}{C_{sw}} - 1 = AC_{sw}^{n}\frac{v\delta}{D} \tag{1.1}$$

The expression given in Eq. 1.2 can be considered a dimensionless velocity term and is the ratio of convection to diffusion where convection contributes to capture, and diffusion contributes to solute dispersion.

$$\frac{v_{ice}\delta}{D} \tag{1.2}$$

By applying a mass balance at the interface, the capture concentration, $C_{i,ice}$, was found using Eq. 1.3.

$$-D\frac{\partial C}{\partial x} = v(C_{i,sw} - C_{i,ice}) \tag{1.3}$$

This mass balance resembles that from Wollhover et al.'s 1985 study but adds an unknown capture concentration, while the interfacial concentration is now represented by the assumed functional form given by Eq. 1.1. Through curve-fitting of experimental data, the authors were able to find appropriate values for A and n. The significant contributions of this study include the postulation of a concentration boundary layer and a functional form for the interfacial concentration. However, by simply assuming an interfacial velocity and neglecting heat transfer, the model was not predictive of the ice growth rate.

In an experimental study of freeze concentration by Gu et al., the partition coefficient, defined in Eq. 1.4, was evaluated for various ice growth rates [18]. Note that the volume averaged solute concentration in the ice, C_{ice}, is distinct from the time-dependent concentration in the interfacial solid, $C_{i,ice}$.

$$K = \frac{C_{ice}}{C_{sw}} \tag{1.4}$$

As expected, it was found that a greater ice growth rate resulted in a greater partition constant. Notably, it was found that, by extrapolating the relationship between growth velocity and partition coefficient, a growth velocity of zero corresponded to a non-zero partition coefficient. This suggests that, even for very slow growth rates, freeze concentration will not yield a perfectly pure crystal. Physically, this phenomenon can be explained by the resulting osmotic pressure which would occur between the solute-containing free-stream and a nearly pure interface. To support this explanation, Gu et al. showed that the limiting partition coefficient increased with free-stream concentration.

Because crystal growth is not always planar, it is possible for pockets of brine to become trapped inside the solid phase. To improve the purity of the freeze concentration product, Mandri et al. experimentally investigated the effectiveness of a sweating step after freezing is complete [13]. After salt water had frozen about an immersed, internally cooled cylinder, the bath was drained, and the internal temperature of the cylinder was increased to a temperature still below 0 C. By increasing the ice temperature, regions with high salt concentration melted while regions of higher purity remained frozen. While reducing the effective yield, the addition of a sweating step was shown to substantially improve purity.

Existing heat transfer models can predict the growth rate and energy consumption of FC processes, and mass transfer models have been developed to correlate the growth rate of the interface to the crystal purity. However, there is need for a cohesive model that can

predict each of these phenomena simultaneously. Further, most freeze concentration configurations in the literature consider flat plate or vertical cylinder geometries. No studies, experimental or analytical, have been found which consider horizontal cylinders. However, arrays of horizontal cylinders are commonly used in heat exchangers and existing applications include ice thermal storage systems. An advantage of the horizontal cylinder geometry over vertical cylinders is that the natural convection-based boundary layer thickness does not vary as greatly over the vertical dimension.

In this thesis, an experimentally validated numerical model is developed to predict the growth rate and purity of ice formed on a horizontal cylinder in quiescent saline water. This model can then be used to design and optimize the freeze concentration process for the horizontal cylinder geometry.

1.4 Thesis Mapping

In Chapter 2 of this document, a coupled heat and mass transfer model will be developed considering the formation of ice about a horizontal, internally cooled tube which is immersed in a saltwater bath. The problem will be formulated analytically, and a numerical solution scheme will be proposed. In chapter 3, the experimental apparatus will be described, and the experimental procedures will be outlined. In addition, a series of experiments will be defined to explore the effects of free-stream solute concentration and ice growth rate on the capture concentration. In Chapter 4, the experimental results will be discussed and used to calibrate the model. The accuracy of the best-fit model will be assessed, and the results of the model will be considered. Chapter 5 will conclude this thesis with a summary of key findings and a series of suggestions for further research.

Chapter 2

MODEL DEVELOPMENT

In this chapter a coupled heat and mass transfer model is developed to predict the growth rate and solute capture of a novel freeze concentration process. The configuration will consist of a tube which is immersed in a stagnant saltwater bath. A coolant will be circulated through the interior of the tube, cooling the tube and causing ice formation on its external surface.

2.1 Heat Transfer Model and Moving Boundary

To formulate the problem, consider a single, horizontal cylinder immersed in saltwater as shown in Figure 2.1. The transient heat equation in radial coordinates (Eq. 2.1) is used to describe the temperature profile within a domain consisting of the tube wall and ice ring where α is the thermal diffusivity, R_1 is the inner radius of the tube, R_2 is the outer radius of the tube, and R_{ice} is the outermost radius of the ice layer.

$$\frac{1}{r}\frac{\partial}{\partial r}\left(r\frac{\partial T}{\partial r}\right)=\frac{1}{\alpha}\frac{\partial T}{\partial t}\ \begin{cases}\alpha=\alpha_{tube}\,, R_1\le r\le R_2\\ \alpha=\alpha_{ice}\,,\ R_2<r\le \mathrm{R}_{ice}\end{cases} \tag{2.1}$$

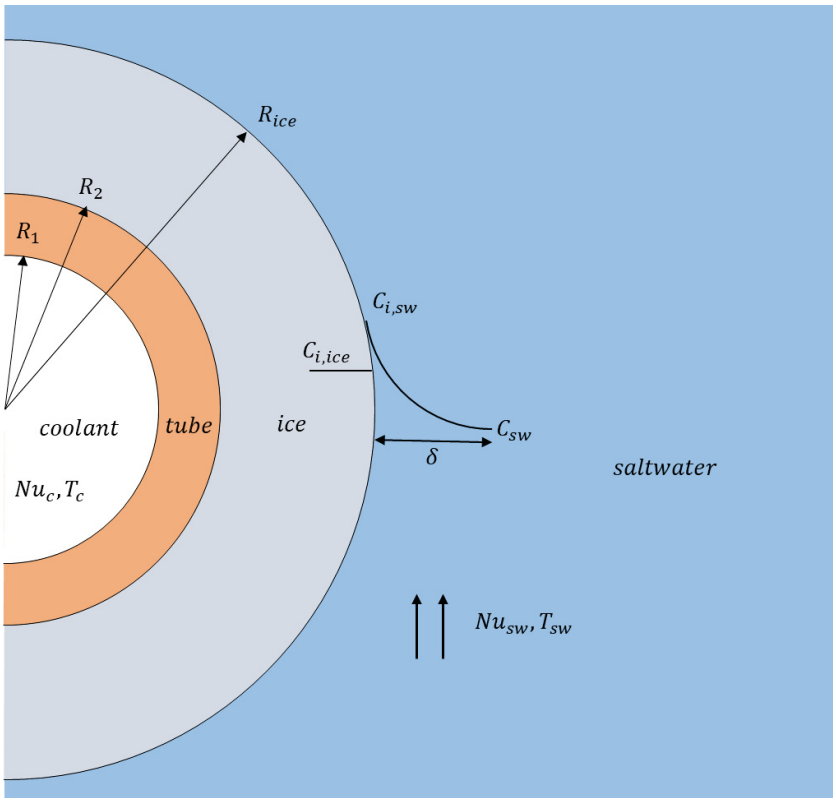

Figure 2.1: Solution domain for radial ice growth and solute rejection around an internally cooled tube.

Uniform natural convection across the exterior ice surface is assumed so that the problem becomes azimuthally symmetric. Although the internal convection coefficient and the coolant's temperature vary significantly in the axial direction, conduction in the axial direction is neglected. This assumption is made because the ice ring's small thickness to length ratio results in a relatively high thermal resistance in the axial direction. Instead, axial effects are accounted for by considering multiple nodes as shown in Figure 2.2 where $T_{c,j}$ is the coolant temperature of node j and J is the total number of axial nodes. No heat or mass transfer occurs between nodes, but each node has a distinct internal convection coefficient as the hydrodynamic and thermal boundary layers develop along the tube length. Additionally, the coolant temperature for a given node increases above

the inlet temperature based on the heat transfer that occurs in upstream nodes. Consequently, the ice radius and temperature and concentration profiles will evolve differently for each node. The solution scheme is the same for each node and downstream nodes depend upon the solutions of upstream nodes through the coolant inlet temperature.

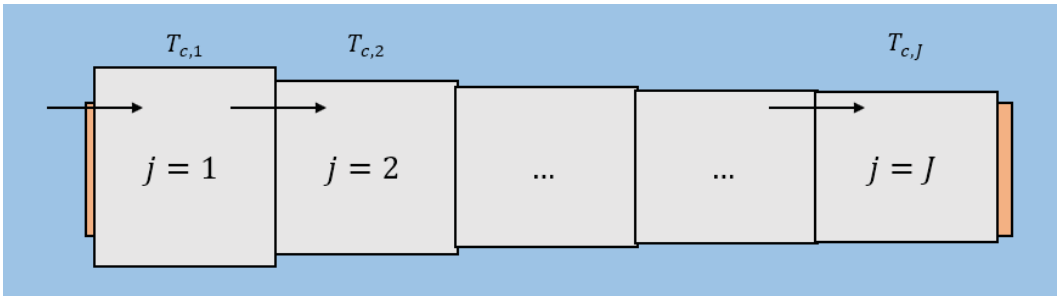

Figure 2.2: Nodal configuration in the axial direction.

The thermal boundary conditions for the heat equation are as follows. The inner surface of the tube is subjected to a convective boundary condition (Eq. 2.2) where k_c is the thermal conductivity of the coolant and Nu is the Nusselt number for the internal flow. The correlation used to determine the internal flow Nusselt number for developing flow in a tube is given in Eq. 2.3 where Gz_d is the Graetz number [19], defined in Eq. 2.4. The tube/ice interface is described by a pair of boundary conditions. Contact resistance is neglected, and the temperatures and heat fluxes on either end of the interface are assumed to be equal (Eqs. 2.5 and 2.6). The final thermal boundary condition, at the outer surface of the ice ring, is a prescribed temperature corresponding to the equilibrium temperature of solidification (Eq. 2.7). This phase change temperature, T_p , is dependent upon the solute concentration in the interfacial liquid, $C_{i,sw}$, and was determined using a fourth order polynomial which was fitted to the water-salt phase diagram by Wollhover et al

[16]. This polynomial is given in Eq. 2.8 where the solute concentration, *C*, is in units of molarity and the temperature is given in units of Kelvin.

$$-k_{tube}\frac{\partial T}{\partial r}|_{R_1} = \frac{Nu_c k_c}{2R_1}(T_c - T|_{R1}) \tag{2.2}$$

$$Nu_c = 3.66 + \frac{0.0668\mathrm{Gz}_d}{1 + 0.04\mathrm{Gz}_d^{2/3}} \tag{2.3}$$

$$\mathrm{Gz}_d = \left(\frac{d}{x}\right)\mathrm{Re}_d\mathrm{Pr} \tag{2.4}$$

$$T|_{R_2^+} = T|_{R_2^-} \tag{2.5}$$

$$-k_{tube}\frac{\partial T}{\partial r}|_{R_2^-} = -k_{ice}\frac{\partial T}{\partial r}|_{R_2^+} \tag{2.6}$$

$$T|_{\mathrm{R}_{ice}} = T_p = f(C_{i,sw}) \tag{2.7}$$

$$T_p(C) = 273.15 - 3.362(C) - 0.0414(C^2) - 0.0404(C^3) - 6.616 * 10^{-4}(C^4) \tag{2.8}$$

Although not used as a thermal boundary condition, the heat transfer at the solid/liquid interface can be further described by considering a correlation for natural convection over a horizontal tube (Eq. 2.9) where $\mathrm{Nu}_{d,sw}$ is the Nusselt number for external convection and Ra_d is the Rayleigh number [20]. The Rayleigh number is defined in Eq. 2.10 where g is the acceleration due to gravity, β is the expansion coefficient, and ν is the kinematic viscosity. This correlation leads to an interfacial heat flux that is distinct from that given by the heat equation solution. The discontinuity in heat fluxes across the outer boundary

is due to the enthalpy of fusion, ΔH_{fus}. Enforcing conservation of energy at the solid/liquid interface leads to Eq. 2.11 where the first term is the conductive heat flux into the interface, the second term is the convective flux associated with the moving interface, and the third term is the convective flux into the adjacent liquid. Rearranging yields an expression for the velocity of the moving boundary (Eq. 2.12).

$$\mathrm{Nu}_{d,sw} = 0.48\ \mathrm{Ra}_d^{\frac{1}{4}} \tag{2.9}$$

$$\mathrm{Ra}_d = \frac{g\beta\left(\mathrm{T_p} - T_{sw}\right)d^3}{\nu\alpha} \tag{2.10}$$

$$-k_{ice}\frac{\partial T}{\partial r}|_{R_{ice}} + v\Delta H_{fus} + \left(T_{sw} - T_p\right)\frac{Nu_{d,sw}k_{sw}}{2R} = 0 \tag{2.11}$$

$$\frac{dR_{ice}}{dt} = v = \frac{k_{ice}\frac{\partial T}{\partial r}|_{R_{ice}} - \left(T_{sw} - T_p\right)\frac{Nu_{d,sw}k_{sw}}{2R}}{\Delta H_{fus}} \tag{2.12}$$

2.2 Mass Transfer Model

To determine the interfacial phase change temperature and the amount of captured solute, it is necessary to model the solute concentration profile near the solid/liquid interface. Initially, the solute is uniformly distributed within the saltwater bath. However, once ice begins to form and solute is rejected due to crystallization, a concentration gradient will develop at the interface. Simultaneously, convective and diffusive forces contribute to solute dispersion. The result is a concentration boundary layer along the outer ice surface.

Beginning with the general form of the radial concentration equation, given in Eq. 2.13, a quasi-steady state profile is assumed. This simplification may be made because of the slow and relatively constant growth rate of the ice front [17]. By modeling the concentration profile only in the radial direction, the azimuthal transport which occurs due to natural convection is neglected.

$$\frac{\partial C}{\partial t} + v\frac{\partial C}{\partial r} = \mathrm{D}\frac{1}{\mathrm{r}}\frac{\partial}{\partial r}\left(r\frac{\partial C}{\partial r}\right) \tag{2.13}$$

The resulting form of the diffusion equation in radial coordinates is given in Eq. 2.14. The domain resides entirely in the saltwater and extends from the solid/liquid interface to the far end of the concentration boundary layer. The concentration profile is visualized in Figure 2.1.

$$D\frac{d^2C}{dr^2} = -\frac{dC}{dr}\left(v + \frac{D}{r}\right) \{R_{ice} \leq r \leq (R_{ice} + \delta) \tag{2.14}$$

The first boundary condition for the concentration profile is a defined but unknown interfacial concentration (Eq. 2.15). The second boundary condition corresponds to the free-stream concentration at the far end of the boundary layer and is given in Eq. 2.16.

$$C(R_{ice}) = C_{i,sw} \tag{2.15}$$

$$C(R_{ice} + \delta) = C_{sw} \tag{2.16}$$

The solute concentration within the interfacial solid phase can be determined by enforcing conservation of mass at the solid/liquid interface. Consider a control volume with an infinitesimal thickness that is fixed to the moving boundary, illustrated in Figure 2.3. This control volume is exposed to two convective fluxes and one diffusive flux where $C_{i,sw}$ is once again the concentration in the interfacial liquid and $C_{i,ice}$ is the concentration in the interfacial solid. By equating the incoming and outgoing fluxes, Eq. 2.17 is derived.

$$-D\frac{dC}{dr}|_{R_{ice}} = v(C_{i,sw} - C_{i,ice}) \tag{2.17}$$

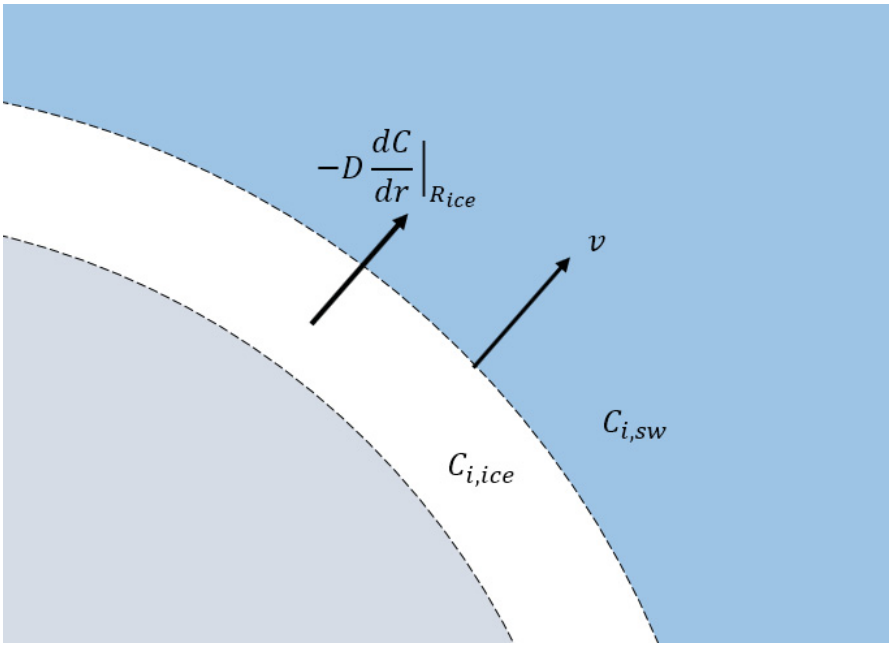

Figure 2.3: Control volume at solid/liquid interface.

Integrating the governing equation (Eq. 2.14) once and applying Eq. 2.17 to solve for the constant of integration yields the following expression for the concentration gradient.

$$\frac{dC}{dr} = \frac{vR_{ice}}{D}e^{\frac{vR_{ice}}{D}}\left(C_{ice} - C_{i,sw}\right)e^{-\frac{vr}{D}}\frac{1}{r} \tag{2.18}$$

Equation 2.18 must be integrated definitely, because the integral of the right-hand side has no analytical solution. Integrating across the boundary layer yields Eq. 2.19. Using the previously established definition for $C(\delta)$ and rearranging yields an expression for $C_{i,ice}$ in Eq. 2.20.

$$C_{sw} - C_{i,sw} = \frac{vR_{ice}}{D} e^{\frac{vR_{ice}}{D}} \left(C_{i,ice} - C_{i,sw}\right) \int_{R_{ice}}^{R_{ice}+\delta} e^{-\frac{vr}{D}} \frac{1}{r}\, dr \tag{2.19}$$

$$C_{i,ice} = C_{i,sw} - \frac{\left(C_{i,sw} - C_{sw}\right)}{\frac{vR_{ice}}{D} e^{\frac{vR_{ice}}{D}} \int_{R_{ice}}^{R_{ice}+\delta} e^{-\frac{vr}{D}} \frac{1}{r}\, dr} \tag{2.20}$$

This expression for $C_{i,ice}$ is not yet useful as $C_{i,sw}$ and δ are yet to be determined. A functional form for the interfacial concentration, as proposed by Chen and Wu (2015), is given in Eq. 2.21 where A and n are two arbitrary constants which are geometry dependent and were determined for specific systems by fitting to experimental data [17]. Because previous studies found the interfacial concentration to be roughly proportional to the bath concentration ($n \cong 0.25$), the current model was simplified by considering *n* to be zero.

$$C_{i,sw} = C_{sw}\left(1 + AC_{sw}^{n} \frac{v\delta}{D}\right) \tag{2.21}$$

To determine the diffusion boundary layer thickness, δ, Eq. 2.22 is postulated where *b* is an arbitrary coefficient and *Pe* is the Peclet number, defined in Eq. 2.23.

$$\frac{\delta}{R_{ice}} = b(Pe)^{-1/2} \tag{2.22}$$

$$Pe = \frac{vR_{ice}}{D} \tag{2.23}$$

Substituting the Peclet number in Eq. 2.20 and rearranging leads to the following expression for the capture concentration in the ice at the interface.

$$\frac{C_{i,ice}}{C_{sw}} = 1 + Ab\sqrt{Pe} - \frac{Ab(Pe)^{-1/2}e^{-Pe}}{\int_{R_{ice}}^{R_{ice}(1+b(Pe)^{-\frac{1}{2}})} e^{-\frac{vr}{D}}\frac{1}{r}\,dr} \tag{2.24}$$

Similarly, substitution of the Peclet number in Eq. 2.21 yields the following form for the interfacial liquid concentration.

$$C_{i,sw} = C_{sw}\left(1 + Ab\sqrt{Pe}\right) \tag{2.25}$$

These two equations yield the concentrations in the interfacial liquid and solid as a function of the Peclet number, where the interfacial velocity, *v*, which can be found from solution of the heat equation, is the only unknown. The two coefficients, *A* and *b* will be determined by fitting the model to experimental data.

2.3 Numerical Solution Algorithm

The preceding analytical model development has led to formulations of the temperature profile within the solid and the solute concentrations at the interface where the temperature and concentration solutions are coupled by the interfacial velocity. The coupled problems will be solved by discretizing in space and time. To obtain a numerical

solution, a program was written in MATLAB (Appendix B). The solution algorithm is outlined below.

To initialize the heat equation domain, a very small ring of ice (0.3mm thickness) is implemented at the beginning of each simulation. The initial temperature of the tube and ice is uniform and equal to 0 C, as indicated by Eq. 2.26. The growth velocity begins at zero and the liquid interfacial concentration begins at the bath concentration as shown in Eqs. 2.27 and 2.28.

$$T(r, t = 0) = T_p(C = 0) \tag{2.26}$$

$$\frac{dR_{ice}}{dt}(t = 0) = 0 \tag{2.27}$$

$$C_{i,sw}(t = 0) = C_{sw} \tag{2.28}$$

Recalling the quasi-steady state assumption made in the formulation of the concentration equation, it is acceptable to assume that $C(r, t^n) \cong C(r, t^{n-1})$ where *n* is the timestep number. Therefore, the heat equation (Eq. 2.1) can be solved by determining the interfacial temperature, T_p^n, from $C_{i,sw}^{n-1}$. Having solved the heat equation for timestep *n*, the interfacial velocity at the same timestep, *n*, can then be calculated using Eq. 2.12. The interfacial concentrations at the current timestep, $C_{i,sw}^n$ and $C_{i,ice}^n$, are then calculated using $\frac{dR_{ice}}{dt}|^n$ and Eqs. 2.24 and 2.25 before advancing to the next timestep. Thus, a simple marching scheme in time is utilized. The heat equation, a partial differential

equation, was solved with MATLAB's 'pdepe' solver. This solver employs a variable order, implicit scheme.

To select a sufficiently small timestep size, radial node size, and axial node size, the number of nodes in each dimension was doubled until the solution (final ice mass) changed by less than 1 percent. A converged solution was obtained with 25 radial nodes, 4 axial nodes, and a timestep of 4 seconds.

Because the axial nodes only exhibit upstream dependence, the nodal solutions at each timestep are obtained sequentially. Equation 2.29 is used to determine the change in coolant temperature between nodes where ρ_c is the coolant density, $c_{p,c}$ is the coolant specific heat, and $\dot{Q}_c$ is the coolant flowrate. After a solution has been obtained for all nodes, the program advances to the next timestep.

$$T_{c,j+1} = T_{c,j} + \frac{2\pi R_1 k_{tube} L_{tube}}{J \rho_c c_{p,c} \dot{Q}_c} \left[\frac{\partial T}{\partial r} |_{R_1} \right]_j \tag{2.29}$$

To determine the effective capture concentration, it is necessary to store the mass of solute captured during each timestep. The total mass of solute captured during the current timestep is determined by summing over each node using Eq. 2.30.

$$m^n_{NaCl,ice} = \frac{L_{tube}\pi}{J} \sum_{j=1}^{J} \left[C^{n-1}_{i,ice} ((R^n_{ice})^2 - (R^{n-1}_{ice})^2) \right]_j \tag{2.30}$$

When the final timestep is reached, the total mass of ice and the volume averaged capture concentration are determined using Eqs. 2.31 and 2.32.

$$m_{ice} = \frac{\pi L_{tube} \rho_{ice}}{J} \sum_{j=1}^{J} [R^2_{ice} - R^2_2]_j \tag{2.31}$$

$$C_{ice} = \frac{\rho_{ice}}{m_{ice}} \sum_{n=1}^{N} \sum_{j=1}^{J} \left[m_{NaCl,ice}^{n} \right]_j \tag{2.32}$$

The solution algorithm is enumerated below.

1) Solve for temperature in node *j* at timestep *n* using the boundary condition $T_p^n = f\left(C_{i,sw}^{n-1}\right)$ and Eqs. 2.1, 2.2, 2.5-2.7.
2) Calculate the interfacial velocity, $\frac{dR_{ice}}{dt}|^n$, for node *j* using Eq. 2.12.
3) Determine the interfacial concentrations, $C_{i,sw}^n$ and $C_{i,ice}^n$ for node *j* using Eqs. 2.24-2.25.
4) If the current node is not the final node, determine $T_{c,j+1}$ using Eq. 2.29 and repeat steps 1-3 for node *j*+1.
5) Determine the solute mass captured during timestep *n* using Eq. 2.30.

Chapter 3

EXPERIMENTAL APPARATUS AND PROCEDURES

3.1 Experimental Apparatus

To validate the model presented in chapter 2, an experimental apparatus was constructed, and a series of experiments was conducted. The apparatus, depicted in Figure 3.1, consisted of a rectangular tank, a copper cooling tube, and a coolant circulation loop. The apparatus was constructed to allow future testing of an array of 5 tubes in a crossflow configuration. However, for the current project, the array was simplified to a single tube in a quiescent bath. A 5-gallon, polyethylene tank was chosen to contain the saltwater bath and the top surface was cut away to enable access. The tank was kept inside an ice chest to insulate the bath from the atmosphere. An Extech EC170 meter was immersed in the bath to measure the free-stream temperature and salinity during experimental runs.

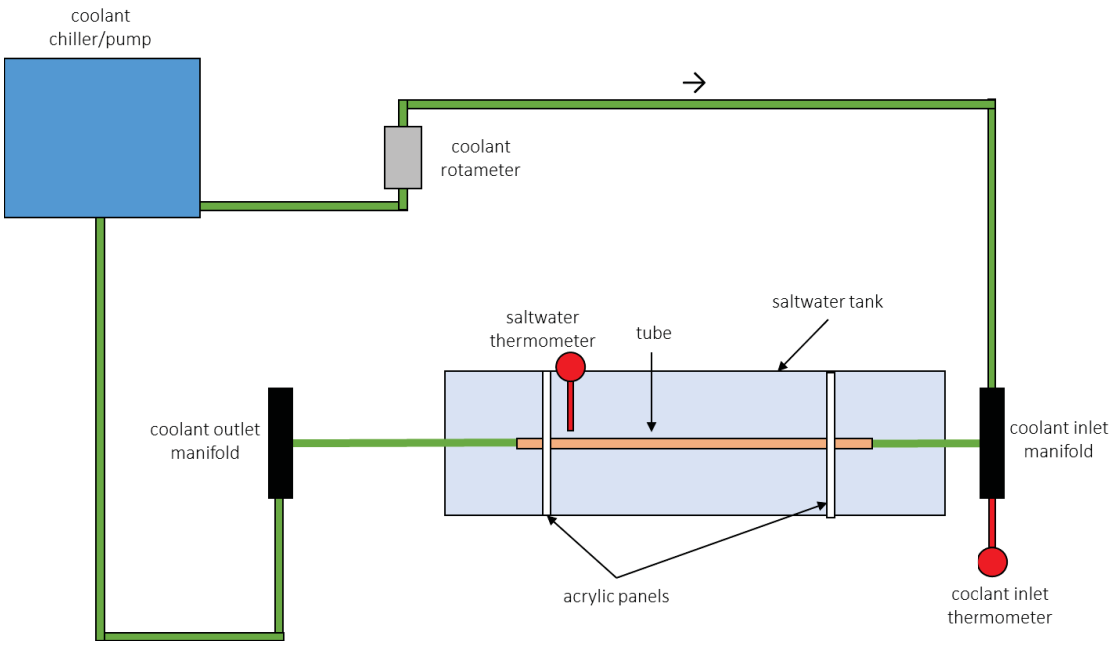

Figure 3.1: Schematic of experimental apparatus.

The copper tube had dimensions as follows: 0.5 inch OD, 0.44 inch ID, and 13 inch length. A foam, insulating ring was inserted on both ends of the tube, and the tube was held in position by two acrylic frames. The foam rings on each end of the tube were used to support the tube in the acrylic frames while allowing for removal after ice growth. The exposed length of the tube was 11.25 inches. Photos of the tank and tube assembly are provided in Figures 3.2 and 3.3.

Figure 3.2: Saltwater tank and tube assembly inside an ice chest.

Figure 3.3: Cooling tube assembly.

A 40%Vol propylene glycol/water mixture was used as the coolant. A Dyneo DD-1000F chiller was used to circulate and cool the working fluid. To measure the flowrate of the coolant, a rotameter was placed between the chiller and the inlet manifold. Due to the highly temperature-dependent viscosity of the propylene glycol mixture, it was found that the rotameter, designed for room temperature water, did not accurately represent the flowrate. By collecting a measured volume of coolant over a specified period of time and comparing the rotameter reading to the directly calculated flowrate, a temperature dependent flow-rate correction factor was developed. The correction factor, defined in Eq. 3.1, is the ratio of the actual flowrate to the meter reading and is plotted vs coolant temperature in Figure 3.4 along with the corresponding uncertainty.

$$\mathrm{Cf} = \frac{\dot{V}}{\dot{V}_{meter}} \tag{3.1}$$

In all experiments, a rotameter reading of 50 gph was used. Uncertainties for the remaining instruments are reported in Table 3.1. To determine the inlet temperature of the coolant, a ThermoWorks reference thermometer was placed on the leading end of the tube. Before each experiment, the bath was pre-cooled to a temperature between 1.5-2.5 C. The bath was stirred while the temperature was being measured to minimize temperature gradients in the bath. Pre-cooling was performed to minimize the change in bath temperature during the experiment and to promote consistency between experiments.

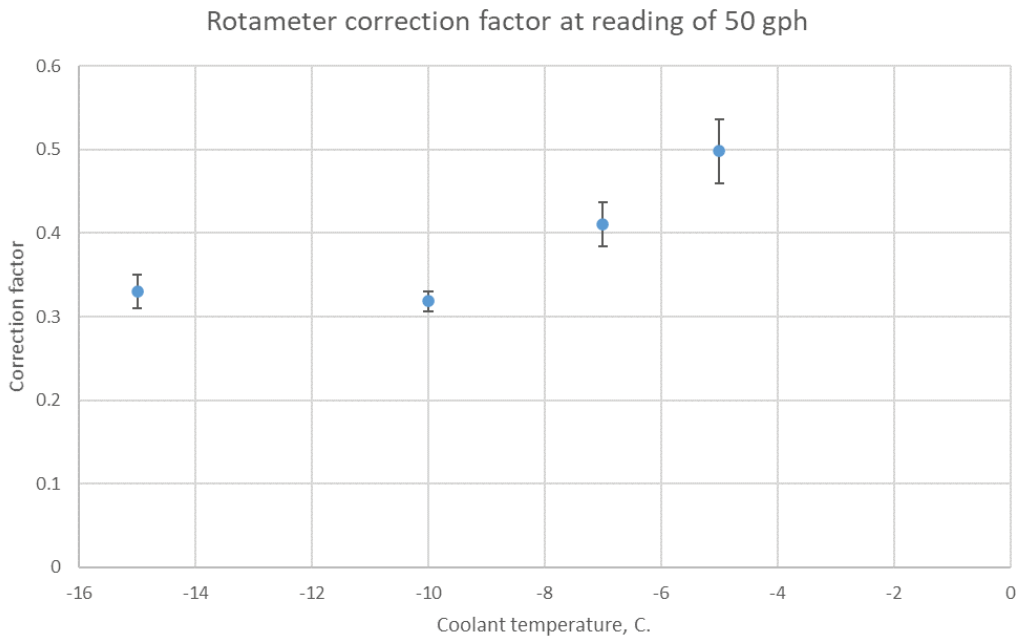

Figure 3.4: Rotameter correction factor vs temperature at a reading of 50 gph.

Table 3.1: Instrument uncertainties.

Instrument	Measurand	Uncertainty
CGOLDENWALL HZ200001B balance	mass of melted ice	+/- 1g
Extech EC170	salinity of saltwater bath and of melted ice	+/- 1.2 ppt
Extech EC170	temperature of saltwater bath	+/- 1 C
ThermoWorks reference thermometer	coolant inlet temperature	+/- 0.03 C

3.2 Experimental Procedures and List of Experiments

For the experimental setup described above, the variable parameters are coolant temperature, bath concentration, and process time. Five experiments each were conducted for sodium chloride bath concentrations of 35 ppt and 20 ppt. For each set of experiments, three coolant temperature (-15 C, -12.5 C, -10 C) were considered for a given process time (30 min) and three process times (30 min, 45 min, 60 min) were considered for a given coolant temperature (-10 C). The initial bath temperature was between 1.5-2.0 C for the 35 ppt set and between 2.0-2.5 C for the 20 ppt set. The offset in initial temperature ranges was chosen due to the difference in the concentration dependent phase change temperature. The selected bath temperatures will result in similar growth velocity ranges across the two data sets.

The input parameters for each experiment are reported in Table 3.2.

Table 3.2: Input parameters for each experiment

Experiment #	Initial bath temperature, C.	Bath concentration, ppt.	Coolant flowrate, gph.	Coolant temperature, C.	Time, min.
1	1.3	35	15.9	-10.0	60
2	1.3	35	15.9	-10.0	45
3	1.3	35	15.9	-10.0	30
4	1.2	35	16.2	-12.5	30
5	1.5	35	16.5	-15.0	30
6	2.3	20	15.9	-10.0	60
7	2.3	20	15.9	-10.0	45
8	2.2	20	15.9	-10.0	30
9	2.3	20	16.2	-12.5	30
10	2.3	20	16.5	-15.0	30

While conducting each experiment, the following procedure was followed.

1. Add sodium chloride to 4-gallon water bath such that the desired salinity is achieved. Pre-cool solution to below the desired temperature.
2. Set desired coolant bath temperature and wait until the bath temperature stabilizes before turning off the coolant chiller.
3. Fill tank with the saltwater solution and stir until the desired starting temperature is reached.
4. Begin coolant circulation while taking periodic measurements of coolant inlet temperature, and saltwater bath temperature. Data was acquired every 10 minutes.
5. Once the experimental runtime was reached, the saltwater bath was drained and coolant circulation was halted. Next, the cooling tube was detached from the assembly and the insulating rings (along with any ice attached to the insulation) were removed. Any residual cooling fluid was drained from the tube before the tube with the surrounding ice layer was placed in a graduated cylinder.
6. After the ice melted, the tube was removed from the cylinder and the mass of the product solution was measured with the CGOLDENWALL balance. An Extech EC170 meter was used to measure the salinity of the melted ice.

Photos of ice frozen about the cooling tube are provided in Figures 3.5 and 3.6.

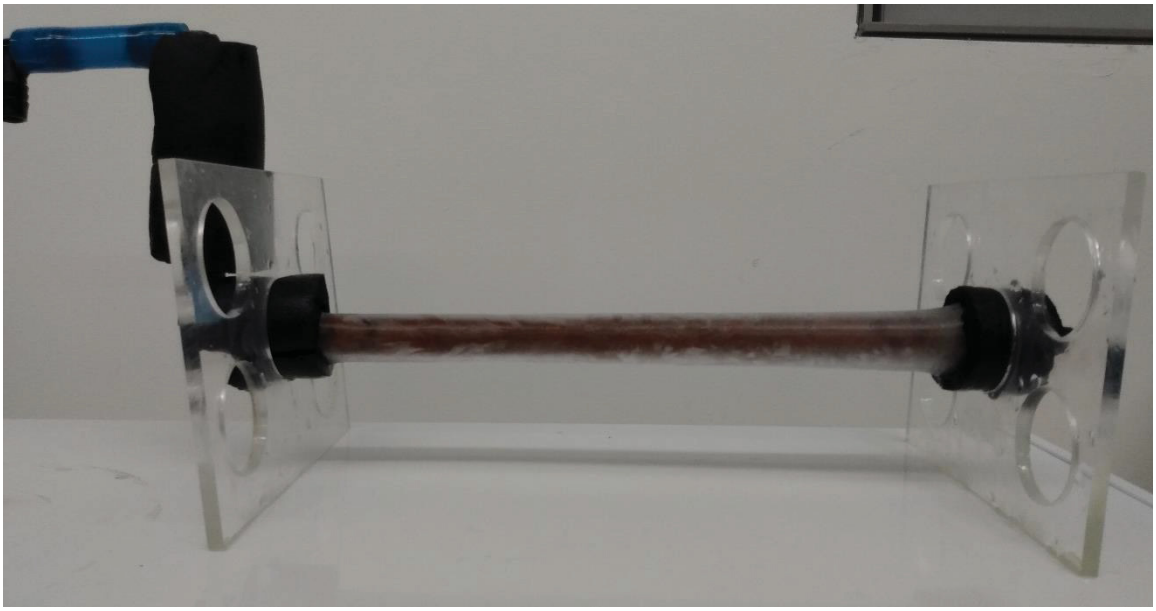

Figure 3.5: Ice about the cooling tube after completion of an experiment.

Figure 3.6: Outer surface of ice after the completion of an experiment.

Chapter 4

RESULTS AND DISCUSSION

This chapter presents and analyzes the results for the ten experiments conducted. This discussion is followed by an explanation of the model calibration procedure. Finally, the results from the fitted model are compared to the experimental results.

4.1 Experimental Results

The mass of ice, effective capture concentration, and partition coefficient from each experiment are reported in Table 4.1 alongside process inputs. Recall that the partition coefficient is the ratio of solute concentration in the ice to solute concentration in the bath. The amount of collected ice ranged from 29.0 – 103.8 grams and the partition coefficient ranged from 0.42 – 0.71.

Table 4.1: Experimentally observed ice mass, capture concentration, and partition coefficient alongside experiment inputs.

Experiment #	Bath concentration, ppt.	Coolant temperature, C.	Time, min.	Ice mass, g.	Capture Concentration, ppt.	Partition coefficient
1	35	-10.0	60	41.0	14.8	0.42
2	35	-10.0	45	35.9	16.4	0.47
3	35	-10.0	30	29.0	19.1	0.55
4	35	-12.5	30	54.3	21.9	0.63
5	35	-15.0	30	67.6	22.9	0.65
6	20	-10.0	60	73.6	9.2	0.46
7	20	-10.0	45	61.4	10.2	0.51
8	20	-10.0	30	42.1	10.8	0.54
9	20	-12.5	30	77.6	13.1	0.66
10	20	-15.0	30	103.8	14.2	0.71

Except for run time, the process inputs of experiments 1-3 were equal with a bath concentration of 35 ppt. The same is true of experiments 6-8 which had a bath concentration of 20 ppt. A comparison of the experiments within each of these sets demonstrates the existence of transient effects. The measured ice masses for these six experiments are plotted in Figure 4.1 and the capture concentrations are plotted in Figure 4.2. Figure 4.1 shows that the mass growth rate decays with time. This phenomenon is a result of the increasing ice thickness. As the ice grows, the conductive thermal resistance increases. In addition, as the external surface area of the ice increases, more heat is introduced from external convection. Finally, it is noted that, although experiments 6-10 (20 ppt) had a higher initial bath temperature, the ice growth rates were greater than those of the analogous 35 ppt experiments. This is due to the concentration dependence of the phase change temperature. A greater bath concentration results in a greater interfacial concentration which, in turn, results in a more significant depression of the freezing point.

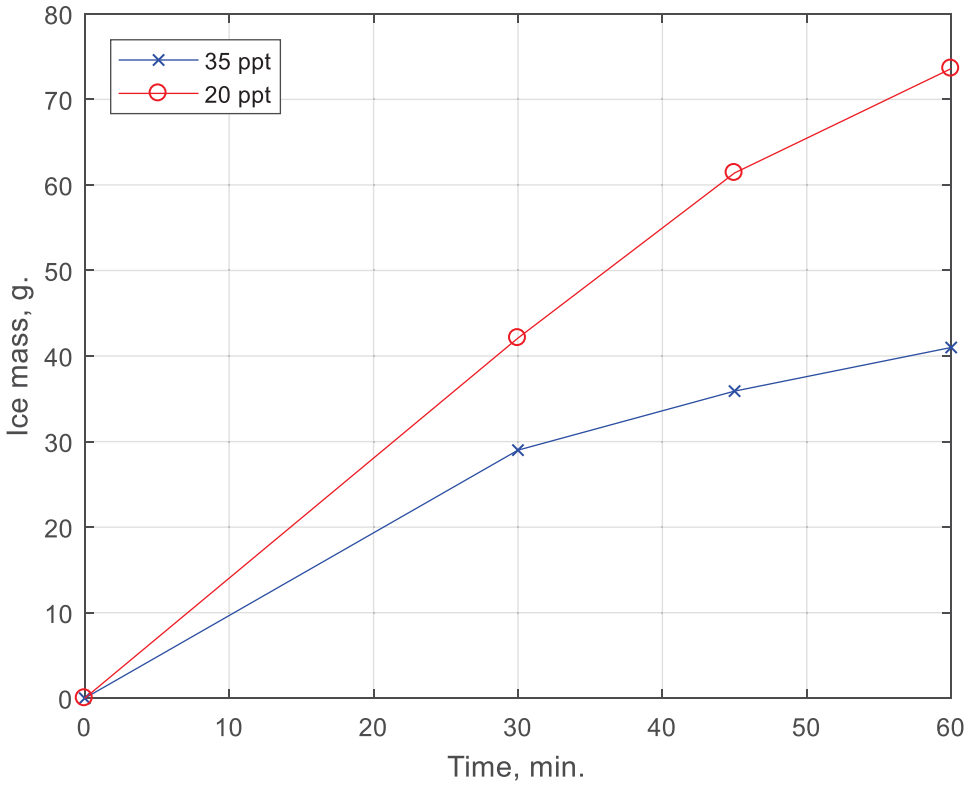

Figure 4.1: Ice mass vs process time for experiments 1-3 (35 ppt) and 6-8 (20 ppt).

As shown in Figure 4.2, the capture concentration decreased with an increasing process time. This reduction demonstrates that the capture concentration decreases with a decrease in the interfacial velocity. To produce ice with uniform salinity using the current system, the coolant temperature would need to be lowered with time to maintain a constant growth velocity in spite of the increasing thermal resistance and surface area of the ice. Regarding process effectiveness, it is interesting to note that, although the average mass growth rates from the experiments were quite low (41-208 g/h), the resultant capture concentration was large. Because fresh water is typically defined as

having less than 1 ppt, the observed purification is not great enough to yield a desirable product.

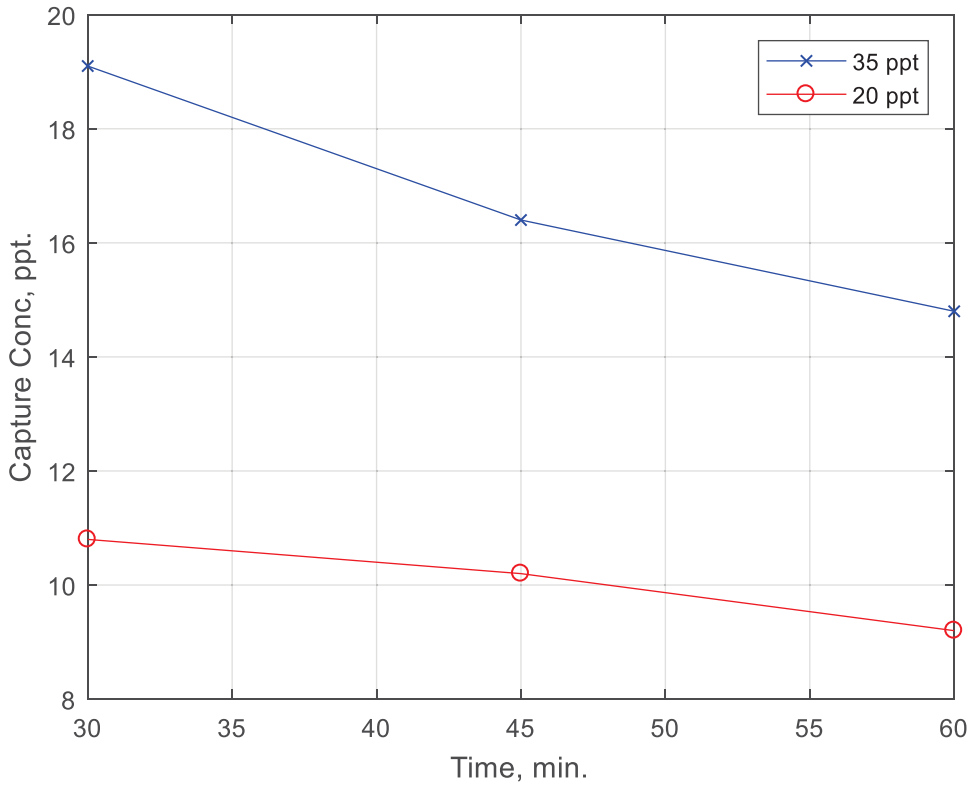

Figure 4.2: Capture concentration vs process time for experiments 1-3 and 6-8.

4.2 Model Calibration

The two coefficients, *A* and *b*, presented during the model development were determined by modeling all 10 experiments with various coefficient combinations until the best fit was achieved. Each coefficient was incremented by a value of 0.05. This step size was small enough to allow for sufficient accuracy, yet large enough to reasonably limit the number of required simulations. By adjusting either coefficient by one step size, the

relative change in model outputs varied by approximately 1 percent. The criteria used to determine best fit was minimization of the residual sum of squares. The residual sum of squares, or RSS, is defined in Eq. 4.1.

$$RSS = \Sigma e_{i,mass}^2 + \Sigma e_{i,conc}^2 \tag{4.1}$$

The model outputs considered in the fitting were ice mass and capture concentration. Since two results were considered for each of ten experiments, the final model represents twenty points fit using two parameters. Because the means and ranges of mass and capture concentration varied significantly from one another, relative error was used when calculating the RSS to ensure that equal weight was assigned to each output. The relative errors are defined in Eqs. 4.2 and 4.3 where *m* is the final ice mass.

$$e_{i,mass} = \left| \frac{m_{i,experiment} - m_{i,model}}{m_{i,experiment}} \right| \tag{4.2}$$

$$e_{i,conc} = \left| \frac{C_{ice\,i,experiment} - C_{ice\,i,model}}{C_{ice\,i,experiment}} \right| \tag{4.3}$$

The coefficient pairing of $A = 0.80$ and $b = 0.20$ resulted in the minimum RSS. As dimensional analysis predicts, the order of magnitude of these values is 1. The resultant model outputs are plotted against the experimentally observed ice mass and capture concentration in Figures 4.3 and 4.4. The R^2 of each fit was 0.95. Outputs of the fitted model are tabulated in Appendix C. Table 4.2 shows the RSS for several coefficient pairings.

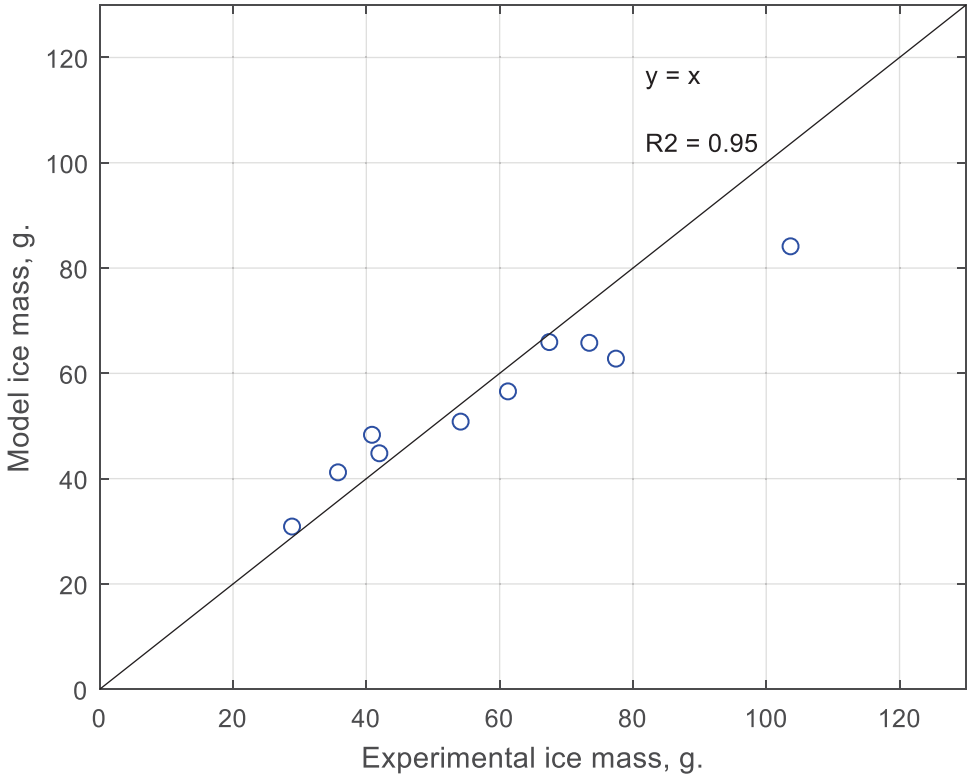

Figure 4.3: Modeled vs observed ice mass for each experiment.

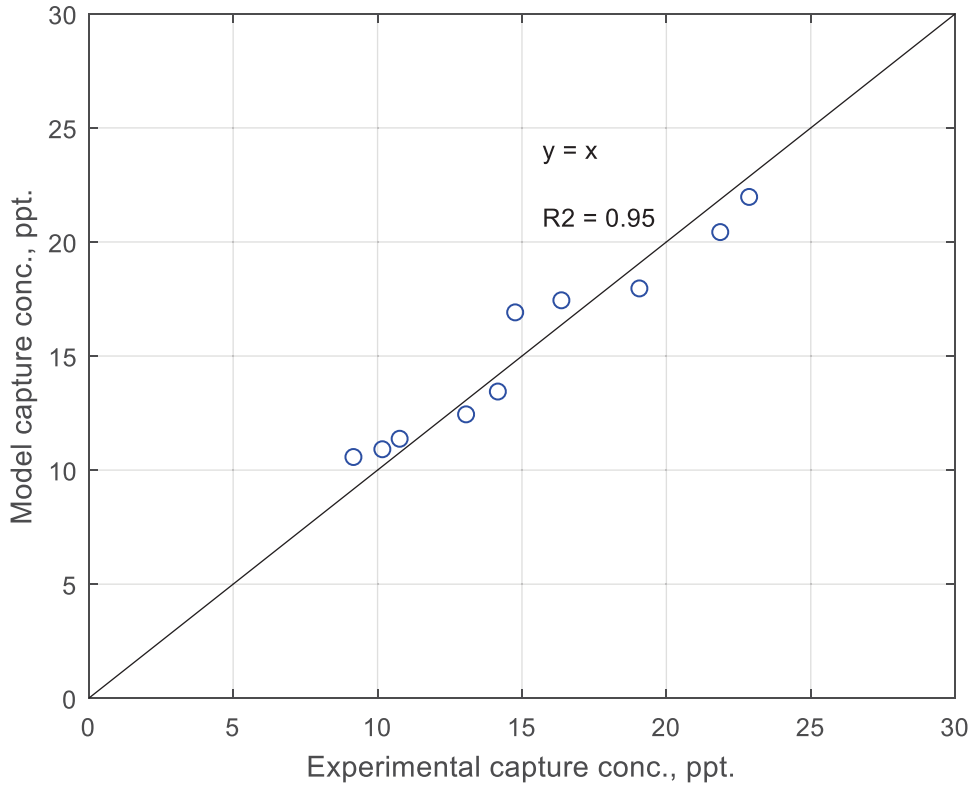

Figure 4.4: Modeled vs observed capture concentration for each experiment.

Table 4.2: Residual sum of squares for various coefficient parings.

	A = 0.75	A = 0.80	A = 0.85
b = 0.15	0.4672	0.4412	0.5512
b = 0.20	0.3401	0.2227	0.2285
b = 0.25	0.5548	0.3856	0.3312

4.3 Model Results

Using the best-fit model configuration, the predicted and observed ice masses and capture concentrations are plotted vs experiment number in Figures 4.5 and 4.6. The root mean square error (RMSE) of ice mass and capture concentration were determined to be 9.01 g and 1.16 ppt respectively. These values correspond to coefficients of variation (CV) of 15.4% and 7.6% respectively. RMSE and CV values were calculated using Eqs. 4.4-4.7.

$$RMSE_m = \sqrt{\frac{\sum_{i=1}^{10}\left(m_{i,experiment} - m_{i,model}\right)^2}{10}} \tag{4.4}$$

$$RMSE_{conc} = \sqrt{\frac{\sum_{i=1}^{10}\left(C_{ice\,i,experiment} - C_{ice\,i,model}\right)^2}{10}} \tag{4.5}$$

$$CV_m = \frac{RMSE_m}{m_{average}} \tag{4.6}$$

$$CV_{conc} = \frac{RMSE_{conc}}{C_{ice\,average}} \tag{4.7}$$

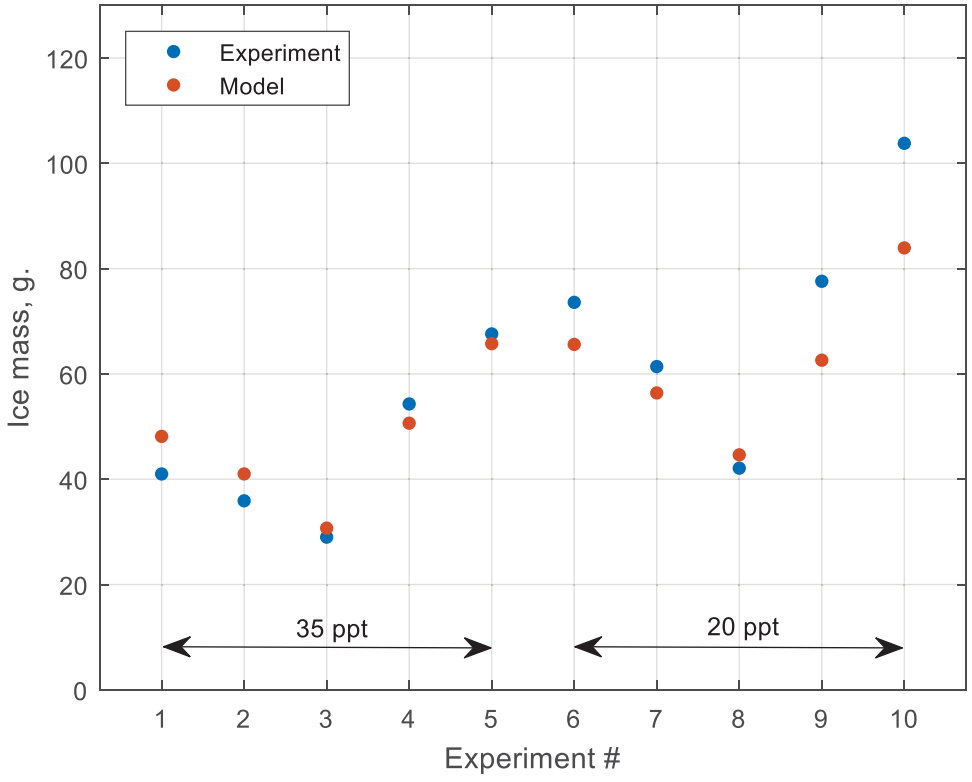

Figure 4.5: Predicted and observed ice mass vs experiment number.

Considering experiments 6-10, the model underpredicts the ice mass for four of the five experiments with a 20 ppt bath concentration. No comparable trend exists in experiments

1-5. This suggests that the ice growth velocity is more dependent upon the bath concentration than the current model predicts. The growth velocity depends upon the interfacial temperature which, in turn, depends upon the interfacial concentration. The expression for interfacial concentration is reiterated in Eq. 4.8.

$$C_{i,sw} = C_{sw}\left(1 + AC_{sw}^{n}\frac{v\delta}{D}\right) \tag{4.8}$$

Recall that, in this work, the exponent *n* was taken to be zero for simplicity. A positive value for *n* in Eq. 4.18 would result in a greater difference in interfacial temperature between the two bath concentrations. This would improve the accuracy of the mass prediction for the 20 ppt cases. However, previous studies have found that a negative value for *n* resulted in the best agreement, although a different geometry and slower growth rate were considered [17].

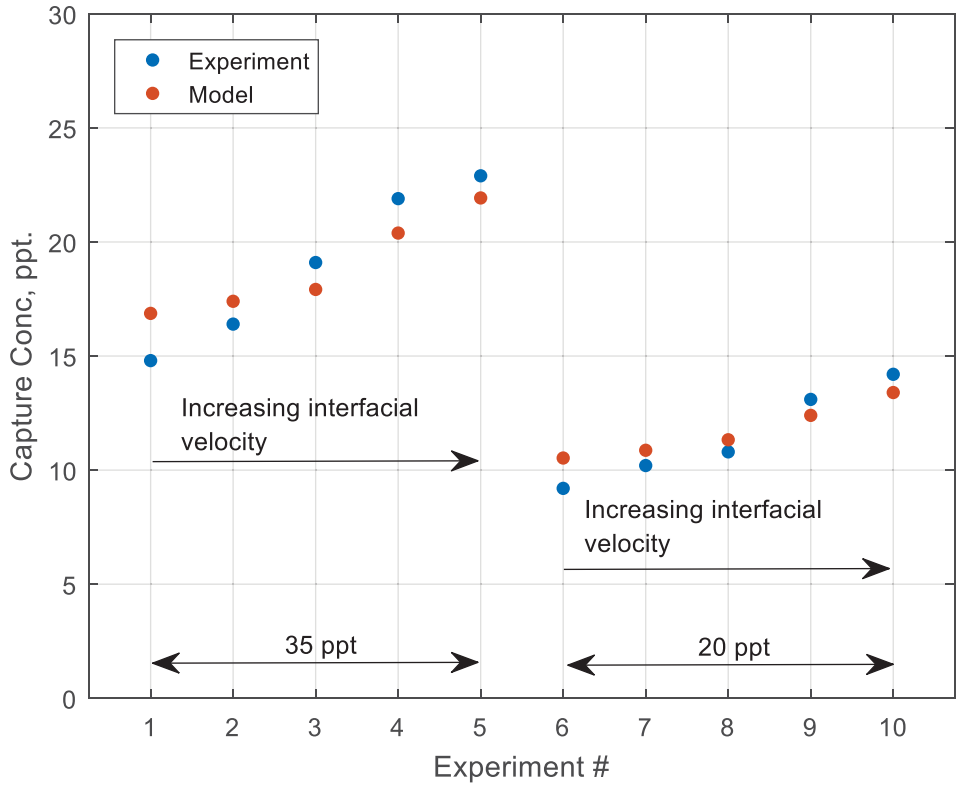

Figure 4.6: Predicted and observed capture concentration vs experiment number.

The predicted capture concentrations, seen in Figure 4.6, are less sensitive to process inputs than the observed capture concentrations. Although the experimental and predicted capture concentrations both increase with growth velocity, the range of model-predicted capture concentrations is much smaller than the range of measured capture concentrations. One possible reason for this discrepancy is the assumption of planar ice growth. In previous experimental studies of freeze concentration, it was found that dendritic ice growth can cause pockets of brine to become trapped in the solid phase [13]. Thus, one would expect the current model, which neglects the effect of dendritic growth, to underpredict capture. Furthermore, if dendritic growth is more pronounced at higher growth rates, the under-prediction would worsen as the ice growth rate increases.

From Eq. 2.24, it can be seen that the Peclet number largely determines the capture concentration. This relationship is illustrated in Figure 4.7 in which the instantaneous partition coefficient is plotted vs the time dependent Peclet number for the simulation results of experiments 1, 5, 6, and 10. Note that, in each simulation, the Peclet number varies with time due to changes in the interfacial velocity and ice radius. The simulations from these experiments were chosen so that the largest range of the Peclet number could be observed. Each simulation's line include data from all four axial nodes. In order to achieve a desirable partition coefficient, the Peclet number must be on the order of 1. One must be careful not to extrapolate far beyond the plotted relationship as previous studies have indicated that a non-zero, limiting partition coefficient exists [18].

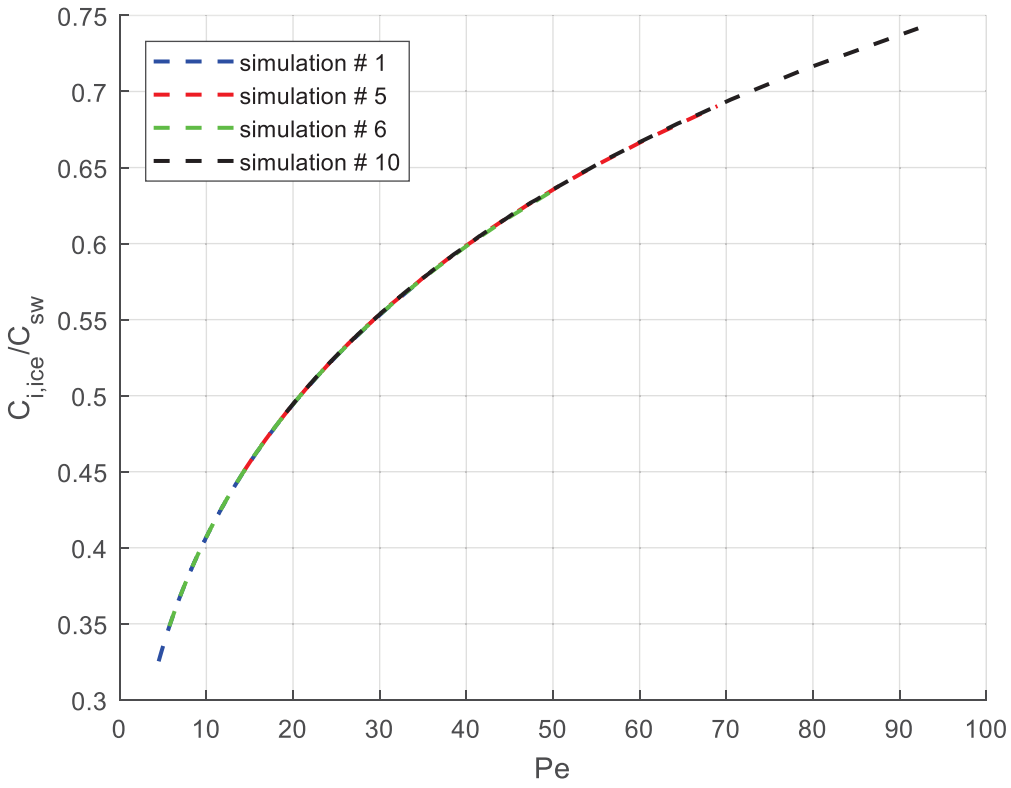

Figure 4.7: Model results for partition coefficient vs Peclet number.

The history of growth velocities for the simulation of experiment 3 is plotted in Figure 4.8. The growth velocity of the entrance node is always larger than that of downstream nodes, but the nodal velocities converge with increasing time. This axial variation is mostly due to the thermally developing flow inside the tube. Because capture concentration is dependent on growth velocity, the present geometric configuration is not optimal. To achieve a desirable capture concentration at the entrance section of the tube, the rate of cooling must be restricted. However, this would result in an unnecessarily low growth velocity at the outlet section of the tube. The thermal entrance length could be reduced by inducing turbulent flow. If this approach is taken, a less viscous coolant should be considered to reduce the flowrate required for turbulence.

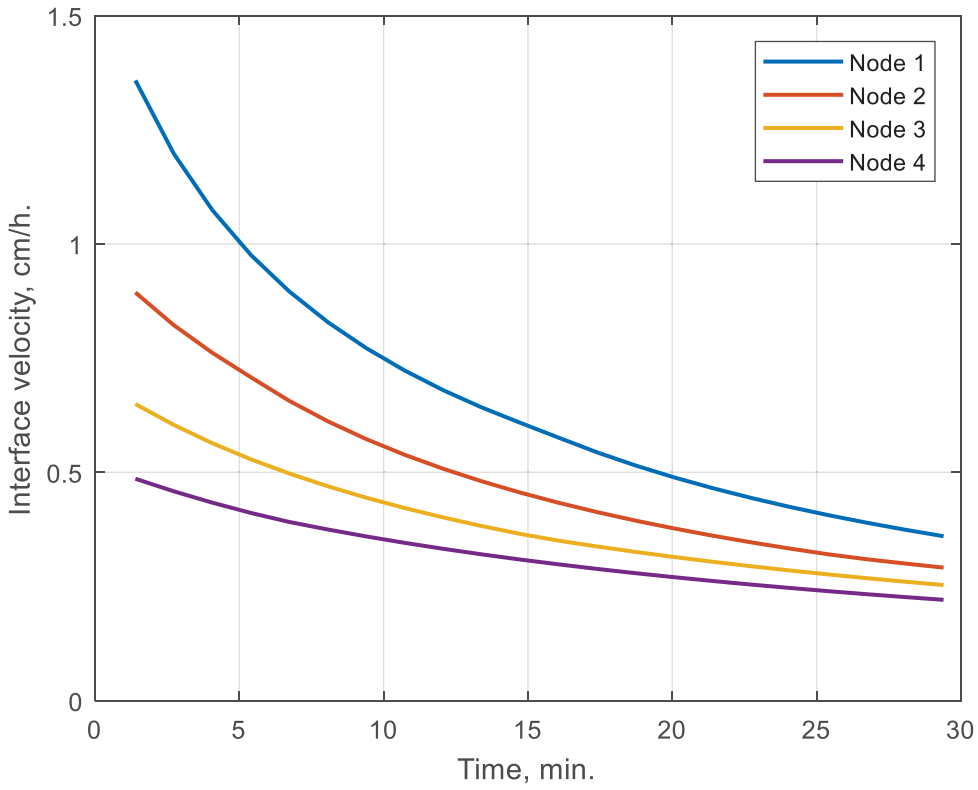

Figure 4.8: Interfacial velocity vs time for the simulation of experiment 3.

Given the temperature of the bath and the temperature profile within the solid, the heat transfer at the boundaries of the ice can be calculated vs time. These heat transfer rates for the simulation of experiment 3 are shown in Figure 4.9. The heat transferred from the bath to the ice was approximately three-fourths of the heat transferred from the ice to the coolant. If only a small fraction of the bath water is frozen, the sensible cooling of the bath translates to wasted energy and the process becomes very energy inefficient. However, if most or all of the bath water is eventually frozen, then the majority of the cooling will have been utilized. Thus, in the design of an effective process it is necessary to maintain a high freezing surface to bath volume ratio.

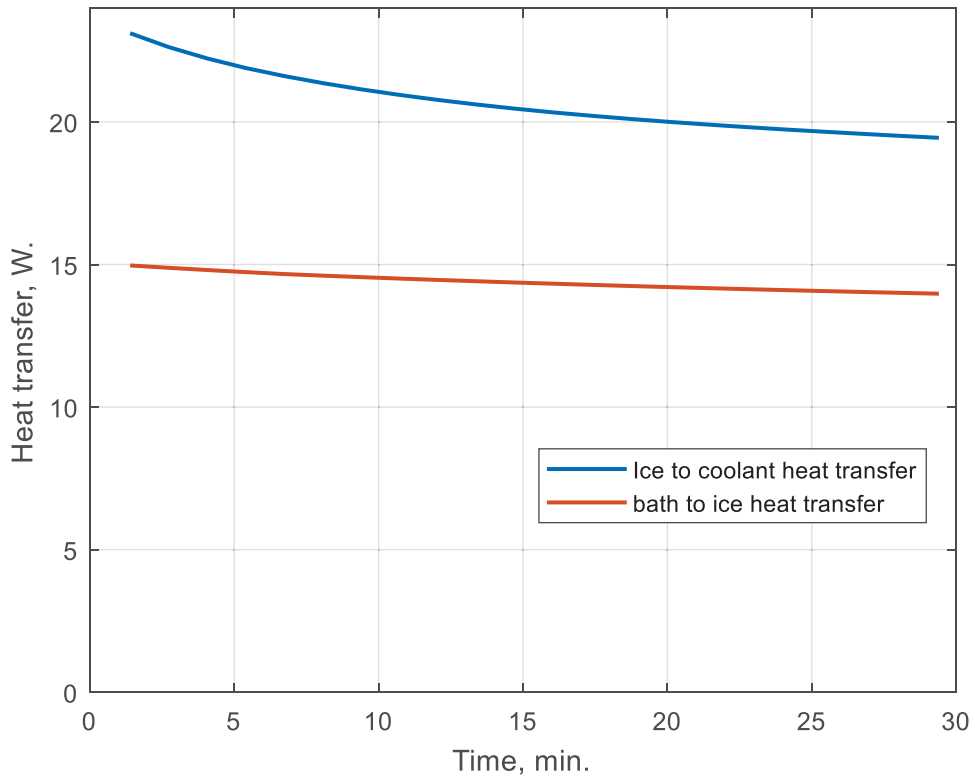

Figure 4.9: Heat transfer at the ice boundaries vs time for the simulation of experiment 3.

Because experimental and simulation results indicated that the product water was too saline to be considered fresh water, the calibrated model was used to simulate a multi-cycle process in which the salinity of the product ice for one stage was used as the bath concentration in the next stage of the cycle. For each stage, the initial bath temperature was 1.5 C, the runtime was 30 minutes, the coolant temperature was -10 C, and the coolant flowrate was 15.9 gph. Nine cycles were necessary to reach a product salinity of less than 1 ppt. The product salinity and ice mass from each cycle are reported in Table 4.3.

Table 4.3: Capture concentration for each cycle in a multi-stage FC process.

Cycle #	Capture Conc, ppt.	Ice mass, g.
1	17.57	28.44
2	10.67	59.43
3	6.87	74.54
4	4.58	85.03
5	3.11	91.77
6	2.14	96.24
7	1.48	99.25
8	1.03	101.33
9	0.72	102.76

Chapter 5

CONCLUSIONS

In this thesis, a coupled heat and mass transfer model was developed to predict the growth of ice about a tube immersed in a saltwater bath. A series of ten experiments was conducted, and the results were used to calibrate the developed model. The model predicted ice mass and capture concentration with coefficients of variation of 15.4% and 7.6% respectively. From experimental and simulation results, the purity of the solid phase was found to be dependent upon the Peclet number. For growth velocities on the order of 10 mm/h, the observed partition coefficient ranged from 0.42-0.71.

The partition coefficients obtained in this study are relatively large and it was found that a single FC cycle at an appreciable growth rate would likely be insufficient to produce fresh water. One way to enhance solute rejection would be to induce forced convection across the outer surface of the tube. Because the capture concentration is primarily determined by the Peclet number, a reduction in the diffusion boundary layer thickness would result in less capture. While cross-flow across the cylinder would reduce the concentration boundary layer thickness, this modification would also accentuate azimuthal asymmetries. A 3-dimensional model may be necessary to accurately represent the forced convection case.

In the present geometric configuration, the thermal resistance and external surface area of the ice both increase with time, resulting in a significant decay in the growth velocity. If ice were instead to be grown inside an externally cooled tube, these two effects would tend to cancel each other, resulting in a more uniform growth velocity. Additionally, if

the tubes were to be immersed in a slowly circulating coolant, the axial variation in growth rate due to thermally developing flow would also be suppressed.

A possible means of improving the energy efficiency of the freeze desalination process is to operate several chambers in tandem in a manner like that of MSF. While ice is being frozen in a given chamber, an adjacent chamber with already-frozen ice could be used as a heat-sink. This low temperature heat sink would result in a significant boost to the refrigeration cycle coefficient of performance. Moving heat to the already-frozen chamber also accelerates the thawing stage.

BIBLIOGRAPHY

[1] Kalista, B., Shin, H., Cho, J., and Jang, A., 2018, "Current Development and Future Prospect Review of Freeze Desalination," Desalination, **447**(July), pp. 167–181.

[2] Al-Karaghouli, A., and Kazmerski, L. L., 2013, "Energy Consumption and Water Production Cost of Conventional and Renewable-Energy-Powered Desalination Processes," Renew. Sustain. Energy Rev., **24**, pp. 343–356.

[3] Miller, J. E., 2003, *Review of Water Resources and Desalination Technologies*.

[4] Zambrano, A., Ruiz, Y., Hernández, E., Raventós, M., and Moreno, F. L., 2018, "Freeze Desalination by the Integration of Falling Film and Block Freeze-Concentration Techniques," Desalination, **436**(February), pp. 56–62.

[5] United States Envitonmental Protection Agency, 1997, "Drinking Water Advisory: Consumer Acceptability Advice and Health Effects Analysis on Methyl Tertiary-Butyl Ether (MTBE)," Off. water, p. EPA-822-F-97-009.

[6] Fipps, G., 2003, "Irrigation Water Quality Standards and Salinity Management Strategies," Texas A&M Agrilife Ext., **4**(03), pp. 1–18.

[7] Shahzad, M. W., Burhan, M., Ang, L., and Ng, K. C., 2017, "Energy-Water-Environment Nexus Underpinning Future Desalination Sustainability," Desalination, **413**, pp. 52–64.

[8] Khawaji, A. D., Kutubkhanah, I. K., and Wie, J. M., 2008, "Advances in Seawater Desalination Technologies," Desalination, **221**(1–3), pp. 47–69.

[9] Kucera, J., 2019, *Desalination 2nd Edition*.

[10] Valladares Linares, R., Li, Z., Yangali-Quintanilla, V., Ghaffour, N., Amy, G., Leiknes, T., and Vrouwenvelder, J. S., 2016, "Life Cycle Cost of a Hybrid Forward Osmosis - Low Pressure Reverse Osmosis System for Seawater Desalination and Wastewater Recovery," Water Res., **88**, pp. 225–234.

[11] Halde, R., 1980, "Concentration of Impurities by Progressive Freezing," **14**, pp. 575–580.

[12] Hirata, T., Matsuzaki, Y., and Ishikawa, M., 2004, "Ice Formation of Aqueous Solution and Its Removal Phenomena on Vertical Cooled Plate," Heat Mass Transf. und Stoffuebertragung, **40**(11), pp. 829–834.

[13] Mandri, Y., Rich, A., Mangin, D., Abderafi, S., Bebon, C., Semlali, N., Klein, J. P., Bounahmidi, T., and Bouhaouss, A., 2011, "Parametric Study of the Sweating Step in the Seawater Desalination Process by Indirect Freezing," Desalination, **269**(1–3), pp. 142–147.

[14] Miyawaki, O., and Inakuma, T., 2021, "Development of Progressive Freeze Concentration and Its Application: A Review," Food Bioprocess Technol., **14**(1), pp. 39–51.

[15] Williams, P. M., Ahmad, M., Connolly, B. S., and Oatley-Radcliffe, D. L., 2015, "Technology for Freeze Concentration in the Desalination Industry," Desalination, **356**, pp. 314–327.

[16] Wollhöver, K., Körber, C., Scheiwe, M. W., and Hartmann, U., 1985,

"Unidirectional Freezing of Binary Aqueous Solutions: An Analysis of Transient Diffusion of Heat and Mass," Int. J. Heat Mass Transf., **28**(4), pp. 761–769.

[17] Chen, X. D., Wu, W. D., and Chen, P., 2015, "An Analytical Relationship of Concentration-Dependent Interfacial Solute Distribution Coefficient for Aqueous Layer Freeze Concentration," AIChE J., **61**(4), pp. 1334–1344.

[18] Gu, X., Suzuki, T., and Miyawaki, O., 2005, "Limiting Partition Coefficient in Progressive Freeze-Concentration," **70**(9), pp. 546–551.

[19] Incropera, F., Dewitt, D., Bergman, T., and Lavine, A., 2003, *Principles of Heat and Mass Transfer, ISV*, John Wiley & Sons, Inc.

[20] Mitchell, J. W., and Braun, J. E., 2012, *Principles of Heating, Ventilation, and Air Conditioning in Buildings*, Wiley.

Appendix A

NOMENCLATURE

T	temperature		α	thermal diffusivity
C	solute concentration		k	thermal conductivity
r	radial position		ρ	density
t	time		c_p	specific heat
R_{ice}	radius of ice ring		D	mass diffusivity
R_1	inner tube radius		Ra	Rayleigh number
R_2	outer tube radius		Nu	Nusselt number
v	velocity of ice front		Gz	Graetz number
δ	concentration boundary layer thickness		Pr	Prandtl number
H	latent heat		Pe	Peclet number
$\dot{Q}$	volumetric flow rate		m	mass
J	number of axial nodes		L_{tube}	exposed tube length
Superscripts/Subscripts				
sw	liquid phase saltwater (bulk)		*i*	solid/liquid interface
ice	solid phase		*p*	phase change
c	coolant		*fus*	fusion
n	timestep		*j*	axial node

Appendix B

MATLAB PROGRAM

```
% Algorithm
%
% 1) Calculate T_phase using interfacial concentration from previous timestep
% 2) Calculate temperature profile for current timestep using T_phase BC
% 3) Calculate velocity from net heat flux across interface
% 4) Calculate boundary layer thickness and interfacial concentrations from
velocity
% 5) Advance to next timestep
%

function [IceMass, Ciceeffective] =
SoluteInclusion_Final_Ab(expNum,Cinf,Tinfa,Tinlet,endTime,Qcool,Ac,b)
%-------------Begin Code Here------------%
% clear;clc; tic;
%------------------INPUTS----------------%
% Cinf = 35.0; % saltwater bath solute concentration, kg/m3.
global Tinf; Tinf = Tinfa; % saltwater bath temp, C.
% Tinlet = -14.54; % coolant inlet temp, C.
% endTime = 3600*(25/60); % experiment time, s.
% Qcool = 16.5; % coolant flowrate, gph.

dt = 4; % timestep, sec.
nZones = 4; % number of axial zones
global nr; nr = 25; % number of radial nodes
outputFreq = 20;
%----------------------------------------%

%------------Physical Parameters------------
global R1; R1 = 0.436/2*2.54/100; % inner radius of tube, m.
global R2; R2 = 0.5/2*2.54/100; % outer radius of tube, m.
yStart = 1.05*R2; % 1.05*R2; % initial/minimum radius of ice, m.
St = 6.35/100; % vertical distance between tube centers, m.
Sd = St; % diagonal distance between tube centers, m.
Sl = sqrt(3/4)*St; % horizontal distance between rows, m.
Ltube = 11.25*2.54/100; % length of tube, m.
liqVol = 0.003785*4; % volume of water, m^3
ntubes = 1; % 5; % number of tubes in array

%------------Physical Properties------------
% Take properties at 5 C, 40 ppt (MIT seawater)
global alphal; alphal = 0.141E-6; % water thermal diffusivity, m^2/s.
global alphas; alphas = 1.364E-6; % ice thermal diffusivity, m^2/s.
H = 333.7E3; % enthalpy of fusion, J/kg.
global kl; kl = 5.775E-1; % water thermal conductivity, W/(m-K).
global ks; ks = 2.34; % ice thermal conductivity, W/(m-K).
global Dc; Dc = 7.8E-10; % salt diffusivity, m^2/s.
global kCu; kCu = 385; % W/m-K
kinviscl = kvisc(Tinf); % for water, m^2/s.
Pr = kinviscl/alphal; % Prandtl number for saltwater
rhol = 1031.5; % density of salt water at 5 C; kg/m^3.
```

```
rhos = 920; % density of ice at -2 C; kg/m^3.
cpl = 3964.9; % for seawater; J/kg-K.
cps = 2030; % for ice; J/kg-K.

%-------------COOLANT PROPERTIES-------------
% properties at 40% volume propylene glycol / water solution
Tcvec = [-5, -10, -15]; % C
mucvec = [0.01663, 0.023, 0.033]; % coolant viscosity, kg/m/s
rhocvec = [1048.2, 1050, 1051.6]; % coolant density, kg/m^3
cpcvec = [3619, 3603, 3586]; % coolant spec heat, J/kg/K
kcvec = [0.361, 0.356, 0.3586]; % W/m/K
rhoC = interp1(Tcvec,rhocvec,Tinlet);
cpC = interp1(Tcvec,cpcvec,Tinlet);
muC = interp1(Tcvec,mucvec,Tinlet);
global kC; kC = interp1(Tcvec,kcvec,Tinlet);
qC = Qcool/951019.3885; % coolant flow rate, m^3/s.
Uc = qC/(pi*R1^2);
ReCool = Uc*(2*R1)*rhoC/muC;
PrCool = muC*cpC/kC;
global NuCool; NuCool = [];
for i = 1:nZones
    Gz = (2*R1)/(Ltube*i/nZones+2*2.54/100)*ReCool*PrCool;
    Nui(i) = 3.66 + 0.0668*Gz/(1+0.04*Gz^(2/3));
    if i == 1
        NuCool(i) = Nui;
    else
        NuCool(i) = i*Nui(i) - sum(NuCool);
    end
end
global Tcool; Tcool = ones(1,nZones)*(Tinlet);
global nz;

%------------Numerical Model Parameters------------
r = [linspace(R1,R2-(R2-R1)/4,5), linspace(R2,yStart,nr-5)]; r = [r; r];
for i = 1:nZones
    rnew(:,:,i) = r;
end
r = rnew;
index = 0;
global Tinitial;
Tinitial = zeros(nZones,nr) + Tinf;

Beta = IsoExpan(Tinf); % Isobaric expansion coeff.
Ra = 9.81*Beta*abs(Tinf-mean(Tinitial(end))+2)*(2*yStart)^3/kinviscl/alphal;
% Rayleigh number
Ra = Ra*ones(nZones,1);
global Nu;
Nu = 0.48*Ra.^(1/4); Nu = Nu';

deltac = Sd/2*ones(nZones,1);

dydt = zeros(nZones,1);
global tCurrent; tCurrent = 0;

T = [Tinitial; Tinitial];
for i = 1:nZones
```

```
    Tnew(:,:,i) = T;
end
T = Tnew;
n = 1; % time indexing vector
global y; y = yStart*ones(nZones,1);
% history of relevant parameters
timehist = [];
Thist = [];
rhist = [];
Cyhist = [];
Cicehist = [];
dydthist = [];
yhist = [];
deltachist = [];
msalt = zeros(nZones,1); % mass of captured salt
%-----------------Phase I----------------------------
disp('Begin Run');
global TprevShifted;
global Cy; Cy = Cinf*ones(nZones,1); % Concentration of salt in liquid at the
interface
Cice = zeros(nZones,1); % Concentration of salt in solid at the interface
global Tinterface; % Temperature at the interface
while ( tCurrent < endTime ) && (2*y(1,end) < St)
    t = linspace(tCurrent,tCurrent+dt,3);
    n = n + 1;
    y(:,n) = y(:,n-1) + dydt*dt;
    %-gradually reduce coolant temperature--%
    if n <= 10
        Tcool = ones(1,nZones)*(Tinlet)*n/10;
    end
    %---------------------------------------%
    for nz = 1:nZones % iterate across axial zones
        rleft = [linspace(R1,R2-(R2-R1)/4,5), linspace(R2,y(nz,n),nr-5)];
        r(2,:,nz) = rleft;
        % Thermal
        % Tinterface = Tphase(Cice(nz)/58.44);
        Tinterface = Tphase(Cy(nz)/58.44);
        TprevShifted = griddedInterpolant(r(1,:,nz),T(1,:,nz));
        sol = pdepe(1,@Spde,@Sic,@Sbc,rleft,t);
        Tsol = sol(3,:);
        T(2,:,nz) = Tsol;
        % calculate dydt
        netHeat = (T(2,end,nz)-Tinf)*Nu(nz)*kl/2/y(nz,end) + ks*(T(2,end,nz)-
T(2,end-1,nz))/(r(2,end,nz)-r(2,end-1,nz));
        dydt(nz) = netHeat/(H*rhol);
        r(1,:,nz) = r(2,:,nz);
        T(1,:,nz) = T(2,:,nz);
        msalt(nz,n) = msalt(nz,n-1) + max(Cice(nz),0)*pi*( y(nz,n)^2 -
y(nz,n-1)^2 )*Ltube/nZones*ntubes;
        qdot(nz) = -kCu*(T(2,2,nz)-T(2,1,nz))/(r(2,2,nz)-
r(2,1,nz))*Ltube/nZones*ntubes*2*pi*R1;
        Tcool(nz+1) = Tcool(nz) - qdot(nz)*(1/rhoC/cpC/qC);% update based on
qdot
        % calculate mass tranp. for t = n
        if dydt(nz) <= 1E-8
            deltac(nz) = Sd/2;
            Cice(nz) = 0;
```

```
            dydt(nz) = 0;
        else
            deltac(nz) = b*sqrt(Dc*y(nz,n)/dydt(nz));
            Cy(nz) = mean([Cy(nz), Cinf*(1+Ac*dydt(nz)*deltac(nz)/Dc)]);
            rInt = linspace(y(nz,n),y(nz,n)+deltac(nz),20);
            Cice(nz) = Cy(nz) - (Cy(nz)-Cinf)*Dc/dydt(nz)/y(nz,n)*exp(-
dydt(nz)*y(nz,n)/Dc)/trapz(rInt,exp(-dydt(nz)*rInt/Dc)./rInt);
            Cice(nz) = max(Cice(nz),0);
        end
    end
    tCurrent = tCurrent + dt;
    for nz = 1:nZones
        Tfilm = (T(2,end,nz)+Tinf)/2;
        kinviscl = kvisc(Tfilm); % for water, m^2/s.
        Pr = kinviscl/alphal; % Prandtl number for saltwater
        Beta = IsoExpan(Tfilm); % Isobaric expansion coeff.
        Ra(nz) = 9.81*Beta*abs(Tinf-
T(2,end,nz))*(2*y(nz,end))^3/kinviscl/alphal;
    end
    Nu = 0.48*Ra.^(1/4); Nu = Nu';
    % periodically output a log of data
    if rem(n-2,outputFreq) == 0
        fprintf('Currently on timestep %d of %d\n',n-1,2+endTime/dt);
        timehist = [timehist; tCurrent];
        [a, ~, ~] = size(Thist);
        for nz = 1:nZones
            Thist(a+1,:,nz) = T(2,:,nz);
            rhist(a+1,:,nz) = r(2,:,nz);
        end
        Cyhist = [Cyhist, Cy];
        Cicehist = [Cicehist; Cice'];
        yhist = [yhist, y(:,end)];
        dydthist = [dydthist, dydt];
        deltachist = [deltachist, deltac];
    end
end
plot(r(2,:),T(2,:))
xlabel('Position, m.')
ylabel('Temperature, C.')
grid on
Cicehist2 = Cicehist;
for i = 1:length(Cicehist2)
    if Cicehist2(i) < 0
        Cicehist2(i) = 0;
    end
end
Ciceeffective = sum(msalt(:,end))/ntubes/pi/Ltube*nZones/sum(y(:,end).^2-
yStart^2)*rhol/rhos;
IceMass = sum(y(:,end).^2-yStart^2)*pi*Ltube/nZones*rhos*1000;
% simTime = toc
disp('End of Simulation');
titlea = ['exp', expNum, '_Ac',num2str(Ac),'.mat'];
save(titlea);
% End of Solution
end
%%%-----------------------------------------------------%%%
%%%-----------PDE, BC, and IC FUNCTIONS--------------%%%
```

```
%%%-----------------------------------------------------%%%

%-------Heat equation for solid-------%
function [c,f,s] = Spde(x,t,T,dTdx)
    global alphas; global R2;
    global ks; global kCu;
    alphaCu = 1.11E-4;
    if x > R2
        c = ks/alphas;
        f = ks*dTdx;
    else
        c = kCu/alphaCu;
        f = kCu*dTdx;
    end
    s = 0;
end

function [T0] = Sic(x)
    global TprevShifted;
    T0 = TprevShifted(x);
end

function [pl,ql,pr,qr] = Sbc(xl,Tl,xr,Tr,t)
    global R1; global nz; global Tcool; global NuCool; global kC;
    % parameters for glycol convection
    NuGly = NuCool(nz);
    Tin = Tcool(nz);
    % inner wall BC
    pl = Tin - Tl;
    ql = 1/kC*(2*R1)/NuGly;
    % outer wall BC; defined T at outer wall interface
    global Tinterface;
    pr = Tr - Tinterface;
    qr = 0;
end

function [pl,ql,pr,qr] = Sbc2(xl,Tl,xr,Tr,t)
    global R1; global nz; global Tcool; global Nu; global y; global kl;
global NuCool; global Tinf; global kC;
    % parameters for glycol convection
    NuGly = NuCool(nz);
    Tin = Tcool(nz);
    % inner wall BC
    pl = Tin - Tl;
    ql = 1/kC*(2*R1)/NuGly;
    % outer wall BC; conserve heat flux
    pr = Tr - Tinf;
    qr = 1/kl*(2*y(nz,end))/Nu(nz);
end

function [ Tinterface ] = Tphase( x )
% calculates the equilibrium temperature (in C) for a given concentration
Tinterface = -3.362*x-0.0414*x^2-0.0404*x^3-(6.616E-4)*x^4;
end

function [kv] = kvisc(Tf)
```

```
% @ C_inf = 35 ppt
Tvec = [0 10 20 25];
kviscvec = [18.54E-7, 13.60E-7, 10.50E-7, 9.37E-7];
kv = interp1(Tvec,kviscvec,Tf,'linear','extrap');
end

function [Beta] = IsoExpan(Tf)
% @ C_inf = 35 ppt
Tvec = [-5, -4, -3, -2, -1, 0, 1, 2, 3, 4, 5, 6, 7, 8, 9, 10];
rhovec = [1028.222, 1028.234, 1028.231, 1028.212, 1028.179, 1028.131,
1028.071, ...
    1027.997, 1027.910, 1027.812, 1027.701, 1027.578, 1027.445, 1027.300,
1027.144,1026.979];
drho = interp1(Tvec,rhovec,Tf+0.1,'linear','extrap') -
interp1(Tvec,rhovec,Tf-0.1,'linear','extrap');
Beta = abs(1/interp1(Tvec,rhovec,Tf,'linear','extrap')*drho/0.2);
end

function [err] = C99(delta, D, v, y)
dr = delta/30;

rdelta = y:dr:(y+delta);
rinf = y:dr:(y+delta)*3;

err = 0.99 - trapz(rdelta,1./rdelta.*exp(-
v*rdelta/D))/trapz(rinf,1./rinf.*exp(-v*rinf/D));
end
%-----------Last Line of Code-----------------%
```

Appendix C

RESULTS FROM FITTED MODEL

Table C.1: Predicted ice mass and capture concentration from the fitted model.

Simulation #	Ice mass, g.	Capture Concentration, ppt.
1	48.14	16.87
2	41.01	17.40
3	30.71	17.92
4	50.64	20.39
5	65.75	21.93
6	65.61	10.53
7	56.39	10.87
8	44.63	11.33
9	62.61	12.40
10	83.94	13.40